AD-A043 518 MCDONNELL DOUGLAS RESEARCH LABS ST LOUIS MO F/G 20/4
VISCOUS FLOWFIELDS AND AIRFRAME FORCES INDUCED BY TWO-DIMENSION--ETC(U)
MAR 77 D R KOTANSKY, W W BOWER N00014-76-C-0494
UNCLASSIFIED ONR-CR215-246-1 NL

| OF |
AD
A043518

END
DATE
FILMED
9 -77
DDC

REPORT ONR-CR215-246-1

VISCOUS FLOWFIELDS AND AIRFRAME FORCES INDUCED BY TWO-DIMENSIONAL LIFT JETS IN GROUND EFFECT

D.R. Kotansky
W.W. Bower

McDonnell Douglas Research Laboratories
St. Louis, Missouri 63166

CONTRACT N00014-76-C-0494
ONR TASK 215-246

1 March 1977

Interim Technical Report for period 1 February 1976 — 28 February 1977

PREPARED FOR THE

OFFICE OF NAVAL RESEARCH ● 800 N. QUINCY ST. ● ARLINGTON ● VA ● 22217

Change of Address

Organizations receiving reports on the initial distribution list should confirm correct address. This list is located at the end of the report. Any change of address or distribution should be conveyed to the Office of Naval Research, Code 211, Arlington, VA 22217.

Disposition

When this report is no longer needed, it may be transmitted to other organizations. Do not return it to the originator or the monitoring office.

Disclaimer

The findings and conclusions contained in this report are not to be construed as an official Department of Defense or Military Department position unless so designated by other official documents.

Reproduction

Reproduction in whole or in part is permitted for any purpose of the United States Government.

UNCLASSIFIED

SECURITY CLASSIFICATION OF THIS PAGE (When Data Entered)

REPORT DOCUMENTATION PAGE

READ INSTRUCTIONS BEFORE COMPLETING FORM

1. REPORT NUMBER: ONR CR215-246-1

2. GOVT ACCESSION NO.

3. RECIPIENT'S CATALOG NUMBER

4. TITLE (and Subtitle): VISCOUS FLOWFIELDS AND AIRFRAME FORCES INDUCED BY TWO-DIMENSIONAL LIFT JETS IN GROUND EFFECT

5. TYPE OF REPORT & PERIOD COVERED: Interim Technical Report, 1 Feb 76 - 28 Feb 77

6. PERFORMING ORG. REPORT NUMBER

7. AUTHOR(s): D. R. Kotansky, W. W. Bower

8. CONTRACT OR GRANT NUMBER(s): N00014-76-C-0494

9. PERFORMING ORGANIZATION NAME AND ADDRESS: McDonnell Douglas Research Laboratories, McDonnell Douglas Corporation, St. Louis, MO 63166

10. PROGRAM ELEMENT, PROJECT, TASK AREA & WORK UNIT NUMBERS: 61153N-14, RR014-11-84, NR215-246

11. CONTROLLING OFFICE NAME AND ADDRESS: Office of Naval Research, Vehicle Technology Program, Code 211, 800 N. Quincy Street, Arlington, VA 22217

12. REPORT DATE: 1 March 1977

13. NUMBER OF PAGES: 86

14. MONITORING AGENCY NAME & ADDRESS (if different from Controlling Office): 84p.

15. SECURITY CLASS. (of this report): Unclassified

15a. DECLASSIFICATION/DOWNGRADING SCHEDULE

16. DISTRIBUTION STATEMENT (of this Report): Approved for public release; distribution unlimited

RRO1411

17. DISTRIBUTION STATEMENT (of the abstract entered in Block 20, if different from Report)

18. SUPPLEMENTARY NOTES

19. KEY WORDS (Continue on reverse side if necessary and identify by block number)

VTOL lift jet
Ground effect
Viscous flow
Turbulence modeling
Finite-difference methods

20. ABSTRACT (Continue on reverse side if necessary and identify by block number)

The interaction of the lift jets and the ground is an important consideration with regard to the design of VTOL aircraft. A key element of this ground effect problem is turbulent jet entrainment, which causes otherwise static air to be set into motion and leads to aerodynamic loads on airframe surfaces. As a first step toward gaining an understanding of this phenomenon, a theoretical analysis of two-dimensional (planar) turbulent jet impingement flowfields has been undertaken. Lift jets emanating from flat and curved surfaces jets in

next page

DD FORM 1 JAN 73 1473 EDITION OF 1 NOV 65 IS OBSOLETE

405 315

UNCLASSIFIED

SECURITY CLASSIFICATION OF THIS PAGE (When Data Entered)

LB

20. ABSTRACT (Continued)

close ground effect have been modeled using the incompressible Reynolds equations in combination with a one-equation turbulence model. Distributions of the flow properties are computed as functions of Reynolds number based on jet exit properties and height of the jet exit plane above ground.

PREFACE

This interim technical report is an account of the work completed at the McDonnell Douglas Research Laboratories on Viscous Flowfields and Airframe Forced Induced by Two-Dimensional Lift Jets in Ground Effect, Contract No. N00014-76-C-0494, from 1 February 1976 to 28 February 1977. The work was done in the Flight Sciences Department, managed by Dr. R. J. Hakkinen. The principal investigator was Dr. D. R. Kotansky. Dr. W. W. Bower performed the analytical work and the numerical computations. The program monitor was Dr. R. E. Whitehead, Office of Naval Research, Arlington, VA.

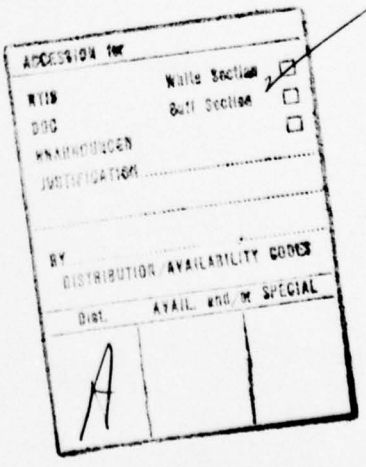

TABLE OF CONTENTS

LIST OF ILLUSTRATIONS

LIST OF TABLES

1. INTRODUCTION

Severe aerodynamic and propulsive interactions occur in the flight of VTOL aircraft during takeoff, landing, and the transition to cruise. In the hover mode, unpredictable forces can be produced on the airframe through the interaction of the lift jets and the ground, a so-called ground effect problem. These forces, which occur as the result of the flow induced by the entrainment of the propulsive lift jets and by the deflected lift jets themselves, can be either positive or negative. In the former case additional lift is provided, but in the latter case, a nominally designed propulsion system may not have sufficient thrust for an adequately controlled takeoff.

The task of determining, either experimentally or theoretically, the aerodynamic and propulsive interference effects of the lift jet, the airframe, and the ground is not a simple one. The numerous variables which affect the flowfield make it economically difficult to study an aircraft configuration through wind tunnel tests alone. On the other hand, the flow is so complex that a rigorous analytical treatment of realistic cases is not possible at the present time.

The objective of the VTOL aircraft flowfield investigation in progress at the McDonnell Douglas Research Laboratories (MDRL) is to predict and compute the flowfield associated with a two-dimensional (planar) lift jet in ground effect. This includes a description of the effect of turbulent jet entrainment on the induced flow and on the static pressure variation over the upper surface from which the jet discharges. The two-dimensional, time-averaged Navier-Stokes equations are presently tractable, and the knowledge gained through their solution for the planar lift jet in ground effect may later be applied to the more complex three-dimensional flowfield problem.

Toward achieving this objective, MDRL has undertaken a combined theoretical and experimental research effort. The initial analytical phase, which was sponsored by the Office of Naval Research (ONR) under the subject contract, is a solution of the two-dimensional, time-averaged conservation equations, in conjunction with a one-equation turbulence model, to describe the turbulent flowfield associated with a single, planar, incompressible lift jet emanating from a static upper surface and impinging on the ground. A planar lift jet permits computation of the vectored configuration since

the flowfield remains two-dimensional, whereas the axisymmetric jet becomes three-dimensional when vectored.

The initial phase of the MDRL experimental effort, which was accomplished under the McDonnell Douglas Independent Research and Development (IRAD) Program, consists of the acquisition of detailed flowfield measurements for the planar jet to establish the validity of the computed flow variables. Although data have been reported for a single axisymmetric jet impinging on a ground plane[1-4], an extensive set of measurements for the planar configuration has not been reported.

This report describes the analytical technique that is used to predict the turbulent flowfields associated with the planar lift-jet/airframe/ground interaction. Computed flow properties are presented as functions of upper-surface geometry, Reynolds number (based on jet exit properties), and jet height above ground. Conclusions are drawn with regard to the accuracy of the flowfield model and the computational technique, and suggestions are made for future study.

2. THE FLOWFIELD MODEL

2.1 The Flow Configuration

The planar impinging jet flow of interest in the present analysis is shown schematically in Figure 1 for the unvectored configuration. The jet exits from a slot of width D in a contoured upper surface a distance H above the ground plane. When the jet impinges normal to the ground, the region of computation extends a distance W on one side of the line of geometric symmetry. When the jet is vectored, the region of interest extends a distance W on both sides of the line of geometric symmetry.

The jet flowfield can be divided into three regions: a free-jet region in which the flow is essentially the same as that of a jet issuing into an unbounded region of the same fluid; the impingement region, in which the flow changes direction with a large pressure gradient; and the wall-jet region in which the flow traverses the surface with zero pressure gradient. The fluid surrounding the jet is entrained at the boundaries of the jet in all three regions, causing otherwise static fluid to be set into motion. On the upper bounding surface, this motion results in locally reduced static pressures and aerodynamic loads.

2.2 The Governing Equations

For the configuration of Figure 1, a rigorous fluid dynamic analysis cannot be made by using purely inviscid-flow calculation techniques, even with the addition of empirical or boundary-layer corrections. In fact, a turbulent boundary-layer procedure along the ground surface cannot simply be patched into an inviscid scheme since there are pressure gradients in both coordinate directions with no single dominant direction of flow. Proper treatment of the problem requires an elliptic solution of the complete flowfield with viscous effects.

In the present approach, the time-averaged continuity and momentum (Navier-Stokes) equations for steady, two-dimensional, incompressible flow are used to describe the mean motion of the fluid. As a result of the averaging procedure, unknown turbulent stress terms arise in the time-averaged momentum equations. To solve for the turbulent shear stress, a turbulent-kinetic-energy equation is used in combination with a constitutive equation that relates the square root of the turbulent kinetic energy to the turbulent viscosity.

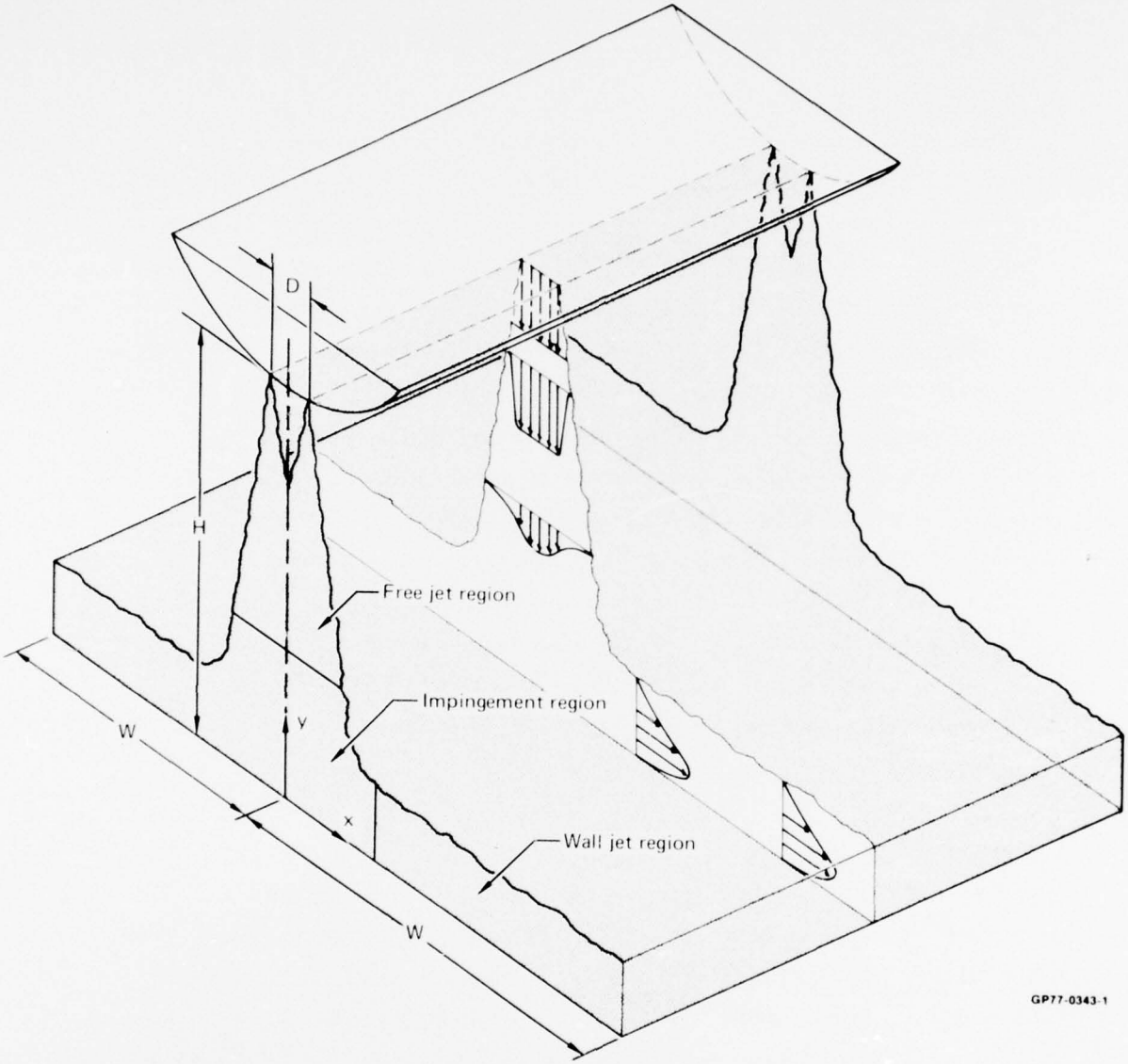

Figure 1 The planar impinging jet

2.2.1 Time-Averaged Primitive Equations

The governing equations for two-dimensional, steady, incompressible flow of a Newtonian fluid with no body forces are those describing the conservation of mass and momentum, written below in tensor notation. Conservation of mass:

$$\frac{\partial \bar{u}_j}{\partial \bar{x}_j} = 0 \quad . \tag{2-1}$$

Conservation of momentum:

$$\bar{\rho}\frac{\partial(\bar{u}_i\bar{u}_j)}{\partial\bar{x}_j} = -\frac{\partial\bar{p}}{\partial\bar{x}_i} + \frac{\partial\bar{\tau}_{ij}}{\partial\bar{x}_j} \quad . \tag{2-2}$$

The stress tensor for incompressible flow is given by:

$$\bar{\tau}_{ij} = \bar{\mu}\left(\frac{\partial\bar{u}_i}{\partial\bar{x}_j} + \frac{\partial\bar{u}_j}{\partial\bar{x}_i}\right) \quad . \tag{2-3}$$

Equations (2-1) through (2-3) are written in terms of the primitive variables of velocity components $\bar{u}_j$, static pressure $\bar{p}$, mass density $\bar{\rho}$, and molecular viscosity $\bar{\mu}$, using a space-fixed reference through which the fluid flows. The overbars in the equations denote that the quantities are dimensional.

To write the time-averaged forms of Equations (2-1) and (2-2) to describe a turbulent flow, the usual Reynolds decomposition is used in which the instantaneous flow variables are expressed as the sum of a mean component and a fluctuating component.

$$\bar{u}_j = \langle\bar{u}_j\rangle + \bar{u}_j' \tag{2-4}$$

$$\bar{p} = \langle\bar{p}\rangle + \bar{p}' \tag{2-5}$$

$$\bar{\tau}_{ij} = \langle\bar{\tau}_{ij}\rangle + \bar{\tau}_{ij}' \quad . \tag{2-6}$$

The symbol $\langle\ \rangle$ denotes a time-averaged component, and the symbol ' denotes a fluctuating component.

With substitution of Equations (2-4) through (2-6) into Equations (2-1) and (2-2), the following time-averaged conservation equations are obtained:

Conservation of mass:

$$\frac{\partial \langle \bar{u}_j \rangle}{\partial \bar{x}_j} = 0 \ . \tag{2-7}$$

Conservation of momentum:

$$\bar{\rho} \frac{\partial \left(\langle \bar{u}_i \rangle \langle \bar{u}_j \rangle \right)}{\partial \bar{x}_j} = - \frac{\partial \langle \bar{p} \rangle}{\partial \bar{x}_i} + \frac{\partial \left(\langle \bar{\tau}_{ij} \rangle - \bar{\rho} \langle \bar{u}_i' \bar{u}_j' \rangle \right)}{\partial \bar{x}_j} \ . \tag{2-8}$$

The form of the time-averaged equation for the conservation of mass, Equation (2-7), is the same as that of the instantaneous equation. The form of the time-averaged equation for the conservation of momentum, Equation (2-8), differs from the instantaneous form through the appearance of the Reynolds stress tensor, $- \bar{\rho} \langle \bar{u}_i' \bar{u}_j' \rangle$. As a result of the latter, the system of Equations (2-7) and (2-8) is not closed. There are one scalar equation, Equation (2-7), and one vector equation, Equation (2-8), but there are the following *unknowns*: one scalar, $\langle \bar{p} \rangle$; one vector, $\langle \bar{u}_j \rangle$; and one tensor, $- \bar{\rho} \langle \bar{u}_i' \bar{u}_j' \rangle$.

2.2.2 Turbulent-Kinetic-Energy Equation

There are five basic turbulence-modeling techniques which can be used to close the system of Equations (2-7) and (2-8). These are described in detail by Reynolds[5] in a current review article and are summarized in Table 1.

The most familiar representation of the turbulence is the so-called zero-equation model in which the Reynolds stress tensor is related to a turbulent (eddy) viscosity, which in turn is related directly to the time-averaged velocity field, generally using a mixing length. This approach has had considerable success in the calculation of boundary layers, as evidenced by the results of Cebeci and Smith[6].

However, the zero-equation model deteriorates in accuracy for flows with significant turning, high entering turbulence levels, stagnation point regions, and boundary layer separation. In the problem under consideration in

the present work, all of these flow phenomena must be taken into account. For this reason, a more complete one-equation model of turbulence has been adopted. In subsequent work, a two-equation model may be adopted if the single equation proves to be unsatisfactory. It should be noted, though, that Reynolds makes the following statement in his review article of Reference 5: "However, it may be that one can do better with this sort of one-equation model in most flows of interest, for it may be easier to specify the length-scale distribution than to compute it with a partial differential equation. This would be particularly true if the length scale really should be governed by the global features of the flow through an integral-differential equation. Hence, further study of one-equation models is encouraged."

TABLE 1 SUMMARY OF TURBULENT-FLOW MODELS BASED ON THE REVIEW BY REYNOLDS[5]

Model type	Essential feature	Advantage	Disadvantage
I Zero-equation	Uses only a pde* for the mean velocity field and no pde's for turbulence quantities	Relatively simple and therefore extremely useful in engineering analysis	Fails to handle some important effects, such as strong surface curvature and freestream turbulence and is inaccurate near separation and in boundary layers with strong accelerations
II One-equation	In addition to a pde for the mean velocity field, uses an additional pde related to the turbulence velocity scale	Describes the dynamics of the turbulence kinetic energy and thereby is more accurate than model type I	Requires knowledge of the turbulence length scale variation throughout the field and requires more computing time than does model type I
III Two-equation	In addition to a pde for the mean velocity field, uses a pde related to the turbulence velocity scale and a pde related to the turbulence length scale	Eliminates the need for specifying the turbulence length scale as a function of position throughout the flow	Fails to produce sufficient anisotropy in the Reynolds stresses for general shear flows and requires more computing time than do model types I and II
IV Stress-equation	In addition to a pde for the mean velocity field, uses pde's for all components of the turbulent stress tensor	Uses exact equations for the turbulent stress tensor which are derived from the Navier-Stokes equations	Presents difficulties in satisfying all the constraints which the terms that are used to compute the turbulent stress tensor must satisfy
V Large-eddy simulations	Uses computation of the three-dimensional time-dependent large-eddy structure and a low-level model for the small-scale turbulence	Eliminates the number of empirical constants which are required	Involves an uncertainty in the effect of the small-scale turbulence modeling on the large-eddy structure and requires relatively large computing times for general shear flows

*Partial differential equation

GP77-0343-2

The essence of the one-equation model is to derive from the instantaneous momentum conservation equations a partial differential equation describing the turbulent kinetic energy of the flow, $\bar{k} = (1/2)\left\langle \bar{u}_j' \bar{u}_j' \right\rangle$. The latter, then, is related through a constitutive equation to the turbulent viscosity and, in turn, to the Reynolds stress.

In the present work, the turbulent-kinetic-energy equation formulated by Wolfshtein[7] is used. To arrive at this equation, it is first necessary to derive an equation for the kinetic energy of the mean motion by adding the scalar product of $\left\langle \bar{u}_j \right\rangle$ and the time-averaged momentum equation for $\left\langle \bar{u}_i \right\rangle$ to the scalar product of $\left\langle \bar{u}_i \right\rangle$ and the time-averaged momentum equation for $\left\langle \bar{u}_j \right\rangle$.

$$\bar{\rho} \frac{\partial\left(\left\langle \bar{u}_i \right\rangle \left\langle \bar{u}_j \right\rangle \left\langle \bar{u}_k \right\rangle\right)}{\partial \bar{x}_k} = - \left\langle \bar{u}_j \right\rangle \frac{\partial \left\langle \bar{p} \right\rangle}{\partial \bar{x}_i} - \left\langle \bar{u}_i \right\rangle \frac{\partial \left\langle \bar{p} \right\rangle}{\partial \bar{x}_j}$$

$$+ \left\langle \bar{u}_j \right\rangle \frac{\partial\left(\left\langle \bar{\tau}_{ik} \right\rangle - \bar{\rho}\left\langle \bar{u}_i' \bar{u}_k' \right\rangle\right)}{\partial \bar{x}_k}$$

$$+ \left\langle \bar{u}_i \right\rangle \frac{\partial\left(\left\langle \bar{\tau}_{jk} \right\rangle - \bar{\rho}\left\langle \bar{u}_j' \bar{u}_k' \right\rangle\right)}{\partial \bar{x}_k} . \qquad (2\text{-}9)$$

When Equation (2-9) is contracted (i = j), the result is the kinetic-energy equation of the mean motion:

$$\bar{\rho} \frac{\partial\left[(1/2)\left\langle \bar{u}_i \right\rangle \left\langle \bar{u}_i \right\rangle \left\langle \bar{u}_k \right\rangle\right]}{\partial \bar{x}_k} = - \left\langle \bar{u}_i \right\rangle \frac{\partial \left\langle \bar{p} \right\rangle}{\partial \bar{x}_i}$$

$$+ \frac{\partial\left[\left\langle \bar{u}_i \right\rangle\left(\left\langle \bar{\tau}_{ik} \right\rangle - \bar{\rho}\left\langle \bar{u}_i' \bar{u}_k' \right\rangle\right)\right]}{\partial \bar{x}_k} \qquad (2\text{-}10)$$

$$+ \bar{\rho}\left\langle \bar{u}_i' \bar{u}_k' \right\rangle \frac{\partial \left\langle \bar{u}_i \right\rangle}{\partial \bar{x}_k} - \left\langle \bar{\tau}_{ik} \right\rangle \frac{\partial \left\langle \bar{u}_i \right\rangle}{\partial \bar{x}_k} .$$

To obtain the equation for the kinetic energy of the turbulent fluctuations, the scalar product of $\bar{u}_j$ and the momentum equation for $\bar{u}_i$ [Equation (2-2)] is added to the scalar product of $\bar{u}_i$ and the momentum equation for $\bar{u}_j$ [Equation (2-2)]. Equations (2-4) through (2-6) are introduced into the resulting equation, which is time-averaged, combined with Equation (2-9), and contracted to give the mean-kinetic-energy equation of the turbulent fluctuations (the so-called turbulent-kinetic-energy equation).

$$\bar{\rho}\,\frac{\partial\left[(1/2)\left\langle \bar{u}_k\right\rangle\left\langle \bar{u}_i'\bar{u}_i'\right\rangle\right]}{\partial \bar{x}_k} + \bar{\rho}\,\frac{\partial\left\langle (1/2)\bar{u}_i'\bar{u}_i'\bar{u}_k'\right\rangle}{\partial \bar{x}_k} = -\left\langle \bar{u}_i'\,\frac{\partial \bar{p}'}{\partial \bar{x}_i}\right\rangle$$

$$+\left\langle \bar{u}_i'\,\frac{\partial \bar{\tau}_{ik}'}{\partial \bar{x}_k}\right\rangle - \bar{\rho}\left\langle \bar{u}_i'\bar{u}_k'\right\rangle\frac{\partial\left\langle \bar{u}_i\right\rangle}{\partial \bar{x}_k}\,. \tag{2-11}$$

By rewriting various derivatives and by introducing the conservation of mass equation and the defining equation for $\bar{\tau}_{ik}$, Equation (2-11) can be shown to be equivalent to the form of the turbulent-kinetic-energy equation used by Wolfshtein[7]:

$$\bar{\rho}\left\langle \bar{u}_j\right\rangle\frac{\partial \bar{k}}{\partial \bar{x}_j} = -\bar{\rho}\left\langle \bar{u}_i'\bar{u}_j'\right\rangle\frac{\partial\left\langle \bar{u}_i\right\rangle}{\partial \bar{x}_j} - \frac{\partial}{\partial \bar{x}_j}\left(\frac{\bar{\rho}\left\langle \bar{u}_j'\bar{u}_i'^{\,2}\right\rangle}{2} - \left\langle \bar{u}_j'\bar{p}'\right\rangle\right)$$

$$+\bar{\mu}\,\frac{\partial^2 \bar{k}}{\partial \bar{x}_j^2} - \bar{\mu}\left\langle\left(\frac{\partial \bar{u}_i'}{\partial \bar{x}_j}\right)^2\right\rangle\,. \tag{2-12}$$

The terms in Equation (2-12) have the following physical meanings:

$\bar{\rho}\left\langle \bar{u}_j\right\rangle\frac{\partial \bar{k}}{\partial \bar{x}_j}$ — Convection of turbulent kinetic energy by the mean motion

$$- \bar{\rho} \left\langle \bar{u}_i' \bar{u}_j' \right\rangle \frac{\partial \left\langle \bar{u}_i \right\rangle}{\partial \bar{x}_j}$$

Production of turbulent kinetic energy

$$- \frac{\partial}{\partial \bar{x}_j} \left(\frac{\bar{\rho} \left\langle \bar{u}_j' \bar{u}_i'^2 \right\rangle}{2} - \left\langle \bar{u}_j' \bar{p}' \right\rangle \right)$$

Turbulent diffusion of turbulent kinetic energy

$$\bar{\mu} \frac{\partial^2 \bar{k}}{\partial \bar{x}_j^2}$$

Viscous diffusion of turbulent kinetic energy

$$- \bar{\mu} \left\langle \left(\frac{\partial \bar{u}_i'}{\partial \bar{x}_j} \right)^2 \right\rangle$$

Viscous dissipation

2.2.3 Wolfshtein's One-Equation Turbulence Model

In order to establish a relation between the various turbulence properties and the turbulent kinetic energy, the turbulence modeling procedure of Wolfshtein[7] will be followed. It is assumed that a scalar turbulent viscosity $\bar{\mu}_{turb}$ can be defined by

$$- \bar{\rho} \left\langle \bar{u}_i' \bar{u}_j' \right\rangle = \bar{\mu}_{turb} \left(\frac{\partial \left\langle \bar{u}_i \right\rangle}{\partial \bar{x}_j} + \frac{\partial \left\langle \bar{u}_j \right\rangle}{\partial \bar{x}_i} \right) , \qquad (2\text{-}13)$$

where the turbulent viscosity is computed from

$$\bar{\mu}_{turb} = c_\mu \bar{\rho} \bar{k}^{1/2} \bar{\ell}_\mu . \qquad (2\text{-}14)$$

In Equation (2-14) c_μ is a constant determined from experiment, $c_\mu = 0.22$, and $\bar{\ell}_\mu$ is the length scale for viscosity.

In addition, it is assumed that the turbulent diffusion of turbulent kinetic energy can be represented by

$$-\frac{\partial}{\partial \bar{x}_j}\left(\frac{\bar{\rho}\left\langle \bar{u}_j'\bar{u}_i'^2\right\rangle}{2}-\left\langle \bar{u}_j'\bar{p}'\right\rangle\right)=\frac{\partial}{\partial \bar{x}_j}\left(\frac{\bar{\mu}_{turb}}{\sigma_{k,turb}}\frac{\partial \bar{k}}{\partial \bar{x}_j}\right). \qquad (2\text{-}15)$$

When Equation (2-15) is added to the viscous diffusion of turbulent kinetic energy $\bar{\mu}(\partial^2\bar{k})/(\partial\bar{x}_j^{\,2})$, the result is

$$\frac{\partial}{\partial \bar{x}_j}\left(\frac{\bar{\mu}_{turb}}{\sigma_{k,turb}}\frac{\partial \bar{k}}{\partial \bar{x}_j}\right)+\bar{\mu}\frac{\partial^2\bar{k}}{\partial \bar{x}_j^{\,2}}=\frac{\partial}{\partial \bar{x}_j}\left[\left(\bar{\mu}+\frac{\bar{\mu}_{turb}}{\sigma_{k,turb}}\right)\frac{\partial \bar{k}}{\partial \bar{x}_j}\right]. \qquad (2\text{-}16)$$

By defining an effective transfer coefficient for the turbulent-kinetic-energy diffusion,

$$\bar{\Gamma}_{k,eff}=\frac{\bar{\mu}}{\sigma_k}+\frac{\bar{\mu}_{turb}}{\sigma_{k,turb}}, \qquad (2\text{-}17)$$

Equation (2-16) can be rewritten as

$$\frac{\partial}{\partial \bar{x}_j}\left[\left(\bar{\mu}+\frac{\bar{\mu}_{turb}}{\sigma_{k,turb}}\right)\frac{\partial \bar{k}}{\partial \bar{x}_j}\right]=\frac{\partial}{\partial \bar{x}_j}\left(\bar{\Gamma}_{k,eff}\frac{\partial \bar{k}}{\partial \bar{x}_j}\right),$$

where σ_k is unity and $\sigma_{k,turb}$ is a constant determined from data, $\sigma_{k,turb}$ = 1.53.

Finally, it is assumed that the viscous dissipation can be represented by

$$\bar{\mu} \left\langle \left(\frac{\partial \bar{u}_i'}{\partial \bar{x}_j} \right)^2 \right\rangle = C_D \frac{\bar{\rho} \bar{k}^{3/2}}{\bar{\ell}_D} \quad . \tag{2-19}$$

C_D is a constant evaluated from data, $C_D = 0.42$, and $\bar{\ell}_D$ is the length scale for dissipation.

When Equations (2-13), (2-18), and (2-19) are substituted into Equation (2-12), the result is

$$\bar{\rho} \langle \bar{u}_j \rangle \frac{\partial \bar{k}}{\partial \bar{x}_j} = \bar{\mu}_{turb} \left(\frac{\partial \langle \bar{u}_i \rangle}{\partial \bar{x}_j} + \frac{\partial \langle \bar{u}_j \rangle}{\partial \bar{x}_i} \right) \frac{\partial \langle \bar{u}_i \rangle}{\partial \bar{x}_j}$$

$$+ \frac{\partial}{\partial \bar{x}_j} \left(\bar{\Gamma}_{k,eff} \frac{\partial \bar{k}}{\partial \bar{x}_j} \right) - C_D \frac{\bar{\rho} \bar{k}^{3/2}}{\bar{\ell}_D} \quad . \tag{2-20}$$

Equation (2-20), the so-called Wolfshtein one-equation turbulence model, is written in terms of the mean velocity field, turbulent kinetic energy, and experimentally determined constants and length scales. The latter will be specified when particular geometries are considered in the analysis.

2.2.4 Non-Dimensional Form of the Time-Averaged Continuity, Momentum, and Turbulent-Kinetic-Energy Equations

Equations (2-7) and (2-8) are written in $\bar{x}$, $\bar{y}$ coordinates with the associated $\bar{u}$, $\bar{v}$ velocity components. The continuity equation has been used in writing the momentum equations in the non-conservation form shown below.

Conservation of mass:

$$\frac{\partial \langle \bar{u} \rangle}{\partial \bar{x}} + \frac{\partial \langle \bar{v} \rangle}{\partial \bar{y}} = 0. \tag{2-21}$$

Conservation of momentum (time-averaged Navier-Stokes or Reynolds equations):
x-momentum equation:

$$\bar{\rho} \langle \bar{u} \rangle \frac{\partial \langle \bar{u} \rangle}{\partial \bar{x}} + \bar{\rho} \langle \bar{v} \rangle \frac{\partial \langle \bar{u} \rangle}{\partial \bar{y}} = - \frac{\partial \langle \bar{p} \rangle}{\partial \bar{x}} + \bar{\mu}_{eff} \frac{\partial^2 \langle \bar{u} \rangle}{\partial \bar{x}^2}$$

$$+ \bar{\mu}_{eff} \frac{\partial^2 \langle \bar{u} \rangle}{\partial \bar{y}^2} + 2 \frac{\partial \langle \bar{u} \rangle}{\partial \bar{x}} \frac{\partial \bar{\mu}_{turb}}{\partial \bar{x}}$$

$$+ \frac{\partial \langle \bar{u} \rangle}{\partial \bar{y}} \frac{\partial \bar{\mu}_{turb}}{\partial \bar{y}} + \frac{\partial \langle \bar{v} \rangle}{\partial \bar{x}} \frac{\partial \bar{\mu}_{turb}}{\partial \bar{y}} . \tag{2-22}$$

y-momentum equation:

$$\bar{\rho} \langle \bar{u} \rangle \frac{\partial \langle \bar{v} \rangle}{\partial \bar{x}} + \bar{\rho} \langle \bar{v} \rangle \frac{\partial \langle \bar{v} \rangle}{\partial \bar{y}} = - \frac{\partial \langle \bar{p} \rangle}{\partial \bar{y}} + \bar{\mu}_{eff} \frac{\partial^2 \langle \bar{v} \rangle}{\partial \bar{x}^2}$$

$$+ \bar{\mu}_{eff} \frac{\partial^2 \langle \bar{v} \rangle}{\partial \bar{y}^2} + \frac{\partial \langle \bar{u} \rangle}{\partial \bar{y}} \frac{\partial \bar{\mu}_{turb}}{\partial \bar{x}} + \frac{\partial \langle \bar{v} \rangle}{\partial \bar{x}} \frac{\partial \bar{\mu}_{turb}}{\partial \bar{x}}$$

$$+ 2 \frac{\partial \langle \bar{v} \rangle}{\partial \bar{y}} \frac{\partial \bar{\mu}_{turb}}{\partial \bar{y}} . \tag{2-23}$$

Defining equations for the turbulent and effective viscosities:

$$\bar{\mu}_{eff} = \bar{\mu} + \bar{\mu}_{turb} \tag{2-24}$$

$$\bar{\mu}_{turb} = c_{\mu} \bar{\rho} \bar{k}^{1/2} \bar{\ell}_{\mu} \ . \tag{2-25}$$

Wolfshtein's one-equation turbulence model, Equation (2-20), takes the following form in the $\bar{x}$-$\bar{y}$ coordinate system:

$$\bar{\rho} \langle \bar{u} \rangle \frac{\partial \bar{k}}{\partial \bar{x}} + \bar{\rho} \langle \bar{v} \rangle \frac{\partial \bar{k}}{\partial \bar{y}} = \bar{\mu}_{turb} \left[2 \left(\frac{\partial \langle \bar{u} \rangle}{\partial \bar{x}} \right)^2 + \left(\frac{\partial \langle \bar{u} \rangle}{\partial \bar{y}} + \frac{\partial \langle \bar{v} \rangle}{\partial \bar{x}} \right)^2 + 2 \left(\frac{\partial \langle \bar{v} \rangle}{\partial \bar{y}} \right)^2 \right] + \frac{\partial}{\partial \bar{x}} \left(\bar{\Gamma}_{k,eff} \frac{\partial \bar{k}}{\partial \bar{x}} \right) + \frac{\partial}{\partial \bar{y}} \left(\bar{\Gamma}_{k,eff} \frac{\partial \bar{k}}{\partial \bar{y}} \right) - C_D \frac{\bar{\rho} \bar{k}^{3/2}}{\bar{\ell}_D} \ . \tag{2-26}$$

With the specification of the length scales, the system of equations is closed, subject to the required boundary conditions.

Equations (2-21) through (2-26) are normalized by introducing the following dimensionless variables:

$$u = \frac{\langle \bar{u} \rangle}{\bar{V}_o} \tag{2-27}$$

$$v = \frac{\langle \bar{v} \rangle}{\bar{V}_o} \tag{2-28}$$

$$\mu_{eff} = \frac{\bar{\mu}_{eff}}{\bar{\rho}\bar{V}_o\bar{D}} \tag{2-29}$$

$$\mu_{turb} = \frac{\bar{\mu}_{turb}}{\bar{\rho}\bar{V}_o\bar{D}} \tag{2-30}$$

$$x = \frac{\bar{x}}{\bar{D}} \tag{2-31}$$

$$y = \frac{\bar{y}}{\bar{D}} \tag{2-32}$$

$$p = \frac{\langle \bar{p} \rangle}{(1/2)\bar{\rho}\bar{V}_o^2} \tag{2-33}$$

$$k = \frac{\bar{k}}{\bar{V}_o^2} \tag{2-34}$$

The dimensionless equations are given below.

Conservation of mass:

$$\frac{\partial u}{\partial x} + \frac{\partial v}{\partial y} = 0 \ . \tag{2-35}$$

x-momentum:

$$u \frac{\partial u}{\partial x} + v \frac{\partial u}{\partial y} = - \frac{1}{2} \frac{\partial p}{\partial x} + \mu_{eff} \left(\frac{\partial^2 u}{\partial x^2} + \frac{\partial^2 u}{\partial y^2} \right) + 2 \frac{\partial u}{\partial x} \frac{\partial \mu_{turb}}{\partial x}$$

$$+ \frac{\partial u}{\partial y} \frac{\partial \mu_{turb}}{\partial y} + \frac{\partial v}{\partial x} \frac{\partial \mu_{turb}}{\partial y} \quad . \tag{2-36}$$

y-momentum:

$$u \frac{\partial v}{\partial x} + v \frac{\partial v}{\partial y} = - \frac{1}{2} \frac{\partial p}{\partial y} + \mu_{eff} \left(\frac{\partial^2 v}{\partial x^2} + \frac{\partial^2 v}{\partial y^2} \right) + \frac{\partial u}{\partial y} \frac{\partial \mu_{turb}}{\partial x}$$

$$+ \frac{\partial v}{\partial x} \frac{\partial \mu_{turb}}{\partial x} + 2 \frac{\partial v}{\partial y} \frac{\partial \mu_{turb}}{\partial y} \quad . \tag{2-37}$$

Wolfshtein one-equation turbulence model:

$$u \frac{\partial k}{\partial x} + v \frac{\partial k}{\partial y} = \mu_{turb} \left[2 \left(\frac{\partial u}{\partial x} \right)^2 + \left(\frac{\partial u}{\partial y} + \frac{\partial v}{\partial x} \right)^2 + 2 \left(\frac{\partial v}{\partial y} \right)^2 \right]$$

$$+ \frac{\partial}{\partial x} \left(\Gamma_{k,eff} \frac{\partial k}{\partial x} \right) + \frac{\partial}{\partial y} \left(\Gamma_{k,eff} \frac{\partial k}{\partial y} \right) - C_D \frac{k^{3/2}}{\ell_D} \, , \tag{2-38}$$

where

$$\mu_{eff} = \frac{1}{Re} + \mu_{turb} \tag{2-39}$$

$$\Gamma_{k,eff} = \frac{1}{\sigma_k Re} + \frac{\mu_{turb}}{\sigma_{k,turb}} \tag{2-40}$$

$$Re = \frac{\bar{\rho}\bar{V}_o\bar{D}}{\bar{\mu}} \quad . \tag{2-41}$$

2.2.5 Vorticity/Stream-Function Form of the Time-Averaged Continuity, Momentum, and Turbulent-Kinetic-Energy Equations

Equations (2-35) through (2-37) are solved in terms of time-averaged vorticity and stream function, which are defined by the following equations:

$$\omega = \frac{\partial v}{\partial x} - \frac{\partial u}{\partial y} \tag{2-42}$$

$$\frac{\partial \psi}{\partial y} = u \tag{2-43}$$

$$\frac{\partial \psi}{\partial x} = - v \quad . \tag{2-44}$$

The relations between the dimensionless and dimensional variables ω and ψ are given by

$$\omega = \frac{\langle \bar{\omega} \rangle}{(\bar{V}_o/\bar{D})} \tag{2-45}$$

$$\psi = \frac{\langle \bar{\psi} \rangle}{\bar{V}_o \bar{D}} \quad . \tag{2-46}$$

The vorticity transport equation is derived by differentiating Equation (2-36) with respect to y, differentiating Equation (2-37) with respect to x, and subtracting the former from the latter.

Vorticity transport equation:

$$(1 + Re\kappa) \frac{\partial^2 \omega}{\partial x^2} - Re \left(\frac{\partial \psi}{\partial y} - 2 \frac{\partial \kappa}{\partial x} \right) \frac{\partial \omega}{\partial x} + (1 + Re\kappa) \frac{\partial^2 \omega}{\partial y^2} + Re \left(\frac{\partial \psi}{\partial x} + 2 \frac{\partial \kappa}{\partial y} \right) \frac{\partial \omega}{\partial y}$$

$$= Re \left[4 \frac{\partial^2 \psi}{\partial x \partial y} \frac{\partial^2 \kappa}{\partial x \partial y} + \frac{\partial^2 \psi}{\partial x^2} \frac{\partial^2 \kappa}{\partial x^2} + \frac{\partial^2 \psi}{\partial y^2} \frac{\partial^2 \kappa}{\partial y^2} - \frac{\partial^2 \psi}{\partial y^2} \frac{\partial^2 \kappa}{\partial x^2} - \frac{\partial^2 \psi}{\partial x^2} \frac{\partial^2 \kappa}{\partial y^2} \right] \quad . \tag{2-47}$$

The following substitution has been made in the previous equation for simplicity of notation:

$$\kappa = \mu_{turb} = c_\mu k^{1/2} \ell_\mu \quad . \tag{2-48}$$

Conservation of mass is ensured through definition of the stream function, which is determined from a Poisson equation as obtained by combining Equations (2-42) through (2-44).

Poisson equation for stream function:

$$\frac{\partial^2 \psi}{\partial x^2} + \frac{\partial^2 \psi}{\partial y^2} = - \omega \quad . \tag{2-49}$$

Equation (2-38) is also written in terms of ω, ψ, and κ.

Wolfshtein turbulence-model equation:

$$\left(\frac{1}{\sigma_k} + \frac{Re\kappa}{\sigma_{k,turb}}\right)\frac{\partial^2 k}{\partial x^2} + Re\left(\frac{1}{\sigma_{k,turb}}\frac{\partial \kappa}{\partial x} - \frac{\partial \psi}{\partial y}\right)\frac{\partial k}{\partial x} + \left(\frac{1}{\sigma_k} + \frac{Re\kappa}{\sigma_{k,turb}}\right)\frac{\partial^2 k}{\partial y^2}$$

$$+ Re\left(\frac{1}{\sigma_{k,turb}}\frac{\partial \kappa}{\partial y} + \frac{\partial \psi}{\partial x}\right)\frac{\partial k}{\partial y} = Re\left\{\frac{C_D k^{3/2}}{\ell_D} - \kappa\left[4\left(\frac{\partial^2 \psi}{\partial x \partial y}\right)^2 + \left(\frac{\partial^2 \psi}{\partial y^2} - \frac{\partial^2 \psi}{\partial x^2}\right)^2\right]\right\}. \tag{2-50}$$

The boundary conditions on ω, ψ, and k which are applied to Equations (2-47), (2-49), and (2-50) are specified when specific geometries are considered.

Once the vorticity, stream function, and turbulent viscosity variations are computed, the velocity component distributions and the static pressure distributions must be calculated. The velocity components are readily obtained from the definition of the stream function, Equations (2-43) and (2-44). The pressure field is computed through a solution of the Poisson equation for pressure. This equation is derived by differentiating Equation (2-36) with respect to x, differentiating Equation (2-37) with respect to y, and adding the two equations.

Poisson equation for static pressure:

$$\frac{\partial^2 p}{\partial x^2} + \frac{\partial^2 p}{\partial y^2} = 4\left[\frac{\partial^2 \psi}{\partial x^2}\frac{\partial^2 \psi}{\partial y^2} - \left(\frac{\partial^2 \psi}{\partial x \partial y}\right)^2 - \frac{\partial \kappa}{\partial x}\frac{\partial \omega}{\partial y} + \frac{\partial \kappa}{\partial y}\frac{\partial \omega}{\partial x}\right.$$

$$\left. + \frac{\partial^2 \psi}{\partial x \partial y}\left(\frac{\partial^2 \kappa}{\partial x^2} - \frac{\partial^2 \kappa}{\partial y^2}\right) - \frac{\partial^2 \kappa}{\partial x \partial y}\left(\frac{\partial^2 \psi}{\partial x^2} - \frac{\partial^2 \psi}{\partial y^2}\right)\right]. \tag{2-51}$$

Equation (2-51) is solved following the solution of Equations (2-47), (2-49), and (2-50); that is, the right-hand-side of the equation is a known quantity. The complexity associated with the solution of the Poisson equation for static pressure is that the magnitude of the pressure is not known at the boundaries. In the present analysis, the pressure level is set at the end point of a boundary, and the momentum equation describing the pressure gradient along the boundary, either Equation (2-22) or Equation (2-23), is integrated to obtain the boundary static pressure variation. The constraints which are imposed on the remaining boundaries are the normal pressure gradients given by the two momentum equations.

3. THE NUMERICAL SOLUTION SCHEME

The coupled, elliptic, partial-differential equations that describe the flow are nonlinear, and a numerical scheme is necessary to obtain a solution. To solve the flowfield equations for a jet discharging from a curved upper surface, a conformal mapping technique is used to map the irregular physical plane into a rectangular computational plane. The governing equations are then rewritten in terms of the computational plane coordinates and solved using finite-difference procedures.

In this section, the conformal mapping and finite-difference techniques are described.

3.1 The Conformal Mapping Technique

To solve the governing equations for a flow with a contoured upper boundary, which simulates the lower surface of a fuselage, an inverse conformal mapping procedure is introduced in the analysis. Details of the mapping procedure and its application to the flowfield equations are given.

3.1.1 Description of the Mapping Procedure

The mapping technique, which was originally devised at MDRL by Hoffman, is best explained with reference to Figure 2. Initially, a finite-difference computational plane with coordinates (ξ,η) is specified. The distance between nodes in the ξ direction is a and in the η direction, b, where a and b are not necessarily equal. Stretching functions are then introduced in each coordinate direction.

$$\mu = f_1(\xi) \tag{3-1}$$

$$\lambda = f_2(\eta) \ . \tag{3-2}$$

With these relations, a mapping plane (μ,λ) is determined which permits finer resolution of the flowfield in regions where the gradients of the computed variables are severe. Finally, a conformal mapping given by

$$\mu + i\lambda = F(x + iy) \tag{3-3}$$

is introduced which specifies the physical plane (x,y). Since the mapping [Equation (3-3)] holds, it follows that both x and y obey Laplace's equation with coordinate stretching.

$$\frac{d\xi}{d\mu}\frac{\partial}{\partial\xi}\left(\frac{d\xi}{d\mu}\frac{\partial y}{\partial\xi}\right) + \frac{d\eta}{d\lambda}\frac{\partial}{\partial\eta}\left(\frac{d\eta}{d\lambda}\frac{\partial y}{\partial\eta}\right) = 0 \tag{3-4}$$

$$\frac{d\xi}{d\mu}\frac{\partial}{\partial\xi}\left(\frac{d\xi}{d\mu}\frac{\partial x}{\partial\xi}\right) + \frac{d\eta}{d\lambda}\frac{\partial}{\partial\eta}\left(\frac{d\eta}{d\lambda}\frac{\partial x}{\partial\eta}\right) = 0. \tag{3-5}$$

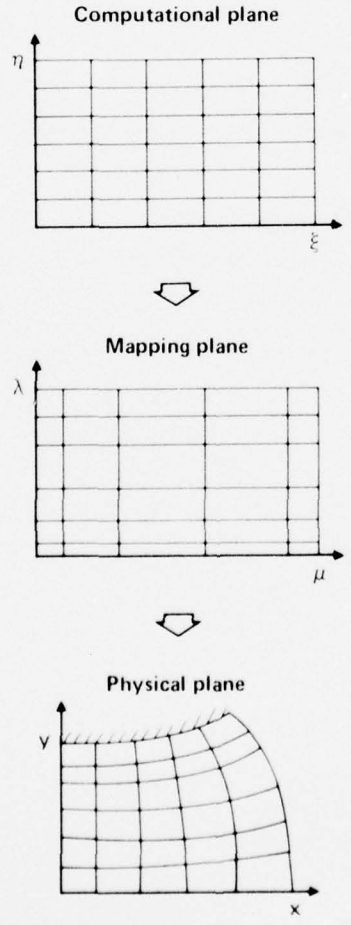

Figure 2 Inverse conformal mapping with stretching

The boundary conditions imposed on Equations (3-4) and (3-5) follow from physical constraints when they are known at the boundaries and from integration of the Cauchy-Riemann relations,

$$\frac{d\xi}{d\mu}\frac{\partial x}{\partial \xi} = \frac{d\eta}{d\lambda}\frac{\partial y}{\partial \eta} \tag{3-6}$$

$$\frac{d\eta}{d\lambda}\frac{\partial x}{\partial \eta} = -\frac{d\xi}{d\mu}\frac{\partial y}{\partial \xi}\,, \tag{3-7}$$

when the x and the y boundary distributions are not known.

The unique feature of the present mapping scheme is that instead of specifying the coordinate distributions in the physical plane and accepting whatever computational plane results, a numerically convenient computational plane is specified, and the corresponding computational mesh within the specified physical boundaries is computed. For this reason, the mapping scheme is an inverse procedure.

Equations (3-4) and (3-5) are discretized in unexpanded form using the central-difference, finite-difference approximations of the derivatives given in Appendix A and the point-of-the-compass grid notation defined in Figure 3. The following forms of Laplace's equation result:

$$L_E y_E + L_W y_W + L_N y_N + L_S y_S - L_P y_P = 0 \tag{3-8}$$

$$L_E x_E + L_W x_W + L_N x_N + L_S x_S - L_P x_P = 0, \tag{3-9}$$

where the coefficients are defined by

$$L_E = \left.\frac{d\xi}{d\mu}\right|_P \left(\left.\frac{d\xi}{d\mu}\right|_P + \left.\frac{d\xi}{d\mu}\right|_E \right) \tag{3-10}$$

$$L_W = \left.\frac{d\xi}{d\mu}\right|_P \left(\left.\frac{d\xi}{d\mu}\right|_P + \left.\frac{d\xi}{d\mu}\right|_W \right) \tag{3-11}$$

$$L_N = g^2 \left.\frac{d\eta}{d\lambda}\right|_P \left(\left.\frac{d\eta}{d\lambda}\right|_P + \left.\frac{d\eta}{d\lambda}\right|_N \right) \tag{3-12}$$

$$L_S = g^2 \left.\frac{d\eta}{d\lambda}\right|_P \left(\left.\frac{d\eta}{d\lambda}\right|_P + \left.\frac{d\eta}{d\lambda}\right|_S \right) \tag{3-13}$$

$$L_P = \left.\frac{d\xi}{d\mu}\right|_P \left(\left.\frac{d\xi}{d\mu}\right|_E + 2 \left.\frac{d\xi}{d\mu}\right|_P + \left.\frac{d\xi}{d\mu}\right|_W \right)$$

$$+ g^2 \left.\frac{d\eta}{d\lambda}\right|_P \left(\left.\frac{d\eta}{d\lambda}\right|_N + 2 \left.\frac{d\eta}{d\lambda}\right|_P + \left.\frac{d\eta}{d\lambda}\right|_S \right) \quad . \tag{3-14}$$

Finite-difference grid parameters

a, b	Normalized grid dimensions in ξ and η directions respectively
$g = a/b$	Ratio of grid dimensions

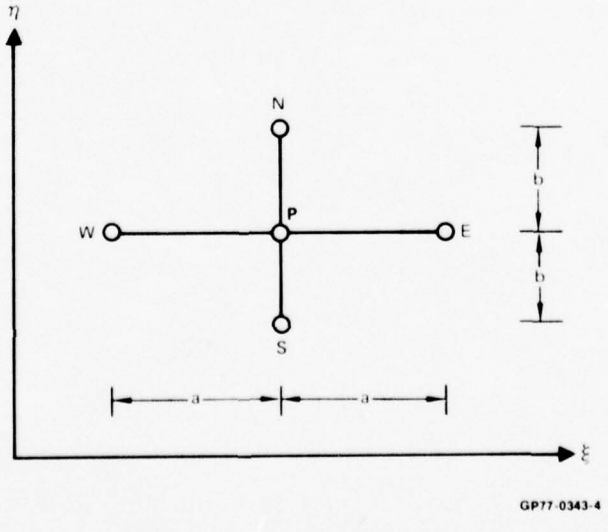

Figure 3 Five-point finite-difference stencil

When boundary distributions of x and y are obtained from the Cauchy-Riemann relations, Equations (3-6) and/or (3-7) are integrated for x and/or y using a second-order-accurate quadrature scheme. Equation (3-8) is solved first for the y field using point relaxation, and then Equation (3-9) is solved for the x field using point relaxation.

In order to determine the accuracy of the numerical mapping procedure, a test case without coordinate stretching was tried for which the relation between the mapping-plane and physical-plane coordinates is known exactly. The problem formulation and the functional relations between (x,y) and (μ,λ) are given in Figure 4(a).

In the numerical solution of Laplace's equation for y, y is specified analytically along the upper and right boundaries. The remaining boundary distributions of y and all the boundary distributions of x are determined from physical constraints or the Cauchy-Riemann relations. The latter are used instead of the analytic boundary values in order to determine the accuracy of the quadrature scheme in computing the boundary conditions.

Figure 4(b) shows the comparison between the exact and numerical mapping for the test case with $\beta = \pi/4$. With a 41 x 41 finite-difference grid, the analytical and numerical mappings agree at worst within 10^{-3}.

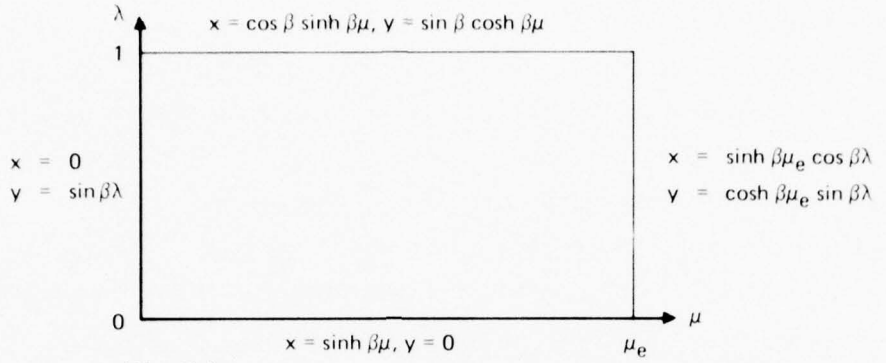

$y + ix = \sin(\beta\lambda + i\beta\mu)$

$x = \cos\beta\lambda \sinh\beta\mu$

$y = \sin\beta\lambda \cosh\beta\mu$

(a) Problem formulation

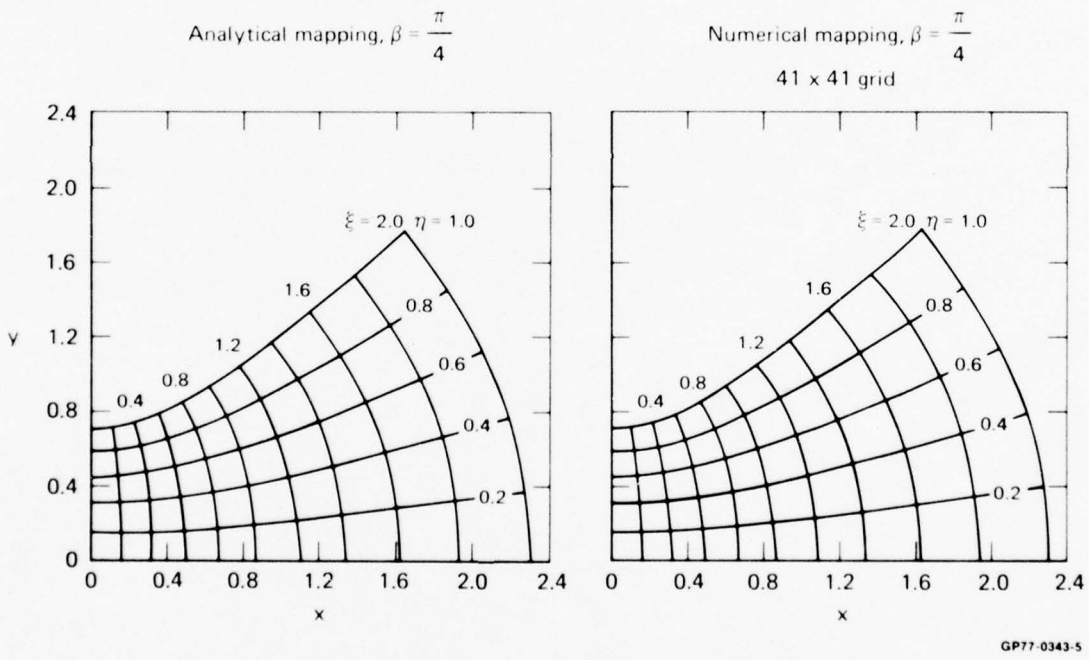

(b) Analytical and numerical mapping solutions

Figure 4 Conformal mapping test case

3.1.2 Application of the Mapping Procedure to the Governing Equations

The time-averaged conservation equations and turbulence-model equation derived in Section 2 which describe a two-dimensional incompressible flow can be written in the Poisson- or transport-equation forms given below.

Poisson equation:

$$\frac{\partial^2 \phi}{\partial x^2} + \frac{\partial^2 \phi}{\partial y^2} = \sigma_P \ . \tag{3-15}$$

For the Poisson equation for stream function, Equation (2-49),

$$\phi = \psi \tag{3-16}$$

$$\sigma_P = - \omega \ , \tag{3-17}$$

and for the Poisson equation for static pressure, Equation (2-51),

$$\phi = p \tag{3-18}$$

$$\sigma_P = 4 \left[\frac{\partial^2 \psi}{\partial x^2} \frac{\partial^2 \psi}{\partial y^2} - \left(\frac{\partial^2 \psi}{\partial x \partial y} \right)^2 - \frac{\partial \kappa}{\partial x} \frac{\partial \omega}{\partial y} + \frac{\partial \kappa}{\partial y} \frac{\partial \omega}{\partial x} \right.$$

$$\left. + \frac{\partial^2 \psi}{\partial x \partial y} \left(\frac{\partial^2 \kappa}{\partial x^2} - \frac{\partial^2 \kappa}{\partial y^2} \right) - \frac{\partial^2 \kappa}{\partial x \partial y} \left(\frac{\partial^2 \psi}{\partial x^2} - \frac{\partial^2 \psi}{\partial y^2} \right) \right] \ . \tag{3-19}$$

Transport equation:

$$\tau_1 \frac{\partial^2 \phi}{\partial x^2} + \tau_2 \frac{\partial \phi}{\partial x} + \tau_1 \frac{\partial^2 \phi}{\partial y^2} + \tau_3 \frac{\partial \phi}{\partial y} = Re \sigma_T \ . \tag{3-20}$$

For the transport equation for vorticity, Equation (2-47),

$$\phi = \omega \tag{3-21}$$

$$\tau_1 = 1 + Re\kappa \tag{3-22}$$

$$\tau_2 = - Re \left(\frac{\partial \psi}{\partial y} - 2 \frac{\partial \kappa}{\partial x} \right) \tag{3-23}$$

$$\tau_3 = Re \left(\frac{\partial \psi}{\partial x} + 2 \frac{\partial \kappa}{\partial y} \right) \tag{3-24}$$

$$\sigma_T = 4 \frac{\partial^2 \psi}{\partial x \partial y} \frac{\partial^2 \kappa}{\partial x \partial y} + \frac{\partial^2 \psi}{\partial x^2} \frac{\partial^2 \kappa}{\partial x^2} + \frac{\partial^2 \psi}{\partial y^2} \frac{\partial^2 \kappa}{\partial y^2}$$

$$- \frac{\partial^2 \psi}{\partial y^2} \frac{\partial^2 \kappa}{\partial x^2} - \frac{\partial^2 \psi}{\partial x^2} \frac{\partial^2 \kappa}{\partial y^2} \quad , \tag{3-25}$$

and for the turbulence-model equation, Equation (2-50),

$$\phi = k \tag{3-26}$$

$$\tau_1 = \frac{1}{\sigma_k} + \frac{Re\kappa}{\sigma_{k,turb}} \tag{3-27}$$

$$\tau_2 = Re \left(\frac{1}{\sigma_{k,turb}} \frac{\partial \kappa}{\partial x} - \frac{\partial \psi}{\partial y} \right) \tag{3-28}$$

$$\tau_3 = \mathrm{Re}\left(\frac{1}{\sigma_{k,\mathrm{turb}}}\frac{\partial \kappa}{\partial y} + \frac{\partial \psi}{\partial x}\right) \tag{3-29}$$

$$\sigma_T = \frac{C_D k^{3/2}}{\ell_D} - \kappa\left[4\left(\frac{\partial^2\psi}{\partial x \partial y}\right)^2 + \left(\frac{\partial^2\psi}{\partial y^2} - \frac{\partial^2\psi}{\partial x^2}\right)^2\right] . \tag{3-30}$$

Applying the conformal mapping procedure with coordinate stretching described in Section 3.1.1, derivatives of a general variable ϕ in the physical plane (x,y) can be expressed in terms of derivatives in the computational plane (ξ,η) with the formulas for $(\partial\phi)/(\partial x)$, $(\partial^2\phi)/(\partial x^2)$, $(\partial\phi)/(\partial y)$, $(\partial^2\phi)/(\partial y^2)$, and $(\partial^2\phi)/(\partial x \partial y)$ given in Appendix B. Using these representations of the derivatives in conjunction with the Cauchy-Riemann relations, Equations (3-15) and (3-20) assume the following forms in the computational plane:
Poisson equation:

$$\left(\frac{d\xi}{d\mu}\right)^2 \frac{\partial^2\phi}{d\xi^2} + \frac{d^2\xi}{d\mu^2}\frac{\partial\phi}{\partial\xi} + \left(\frac{d\eta}{d\lambda}\right)^2 \frac{\partial^2\phi}{\partial\eta^2} + \frac{d^2\eta}{d\lambda^2}\frac{\partial\phi}{\partial\eta} = \frac{\sigma_P}{Q^2} . \tag{3-31}$$

Transport equation:

$$\left[\tau_1\left(\frac{d\xi}{d\mu}\right)^2 Q^2\right]\frac{\partial^2\phi}{\partial\xi^2} + \left[\tau_1\frac{d^2\xi}{d\mu^2}Q^2 + \frac{d\xi}{d\mu}\left(\tau_2\frac{\partial\mu}{\partial x} - \tau_3\frac{\partial\lambda}{\partial x}\right)\right]\frac{\partial\phi}{\partial\xi}$$

$$+ \left[\tau_1\left(\frac{d\eta}{d\lambda}\right)^2 Q^2\right]\frac{\partial^2\phi}{\partial\eta^2} + \left[\tau_1\frac{d^2\eta}{d\lambda^2}Q^2\right.$$

$$\left. + \frac{d\eta}{d\lambda}\left(\tau_2\frac{\partial\lambda}{\partial x} + \tau_3\frac{\partial\mu}{\partial x}\right)\right]\frac{\partial\phi}{\partial\eta} = \mathrm{Re}\sigma_T . \tag{3-32}$$

In these equations, Q is the mapping modulus and is defined by

$$Q^2 = \left(\frac{\partial \mu}{\partial x}\right)^2 + \left(\frac{\partial \mu}{\partial y}\right)^2 = \left(\frac{\partial \lambda}{\partial x}\right)^2 + \left(\frac{\partial \lambda}{\partial y}\right)^2 \quad . \tag{3-33}$$

Equation (3-33) is not convenient for the numerical calculation of Q^2 because (x,y) are solved in terms of (ξ,η). What is needed is Q in terms of the derivatives $[(\partial x)/(\partial \xi), (\partial x)/(\partial \eta)]$ or $[(\partial y)/(\partial \xi), (\partial y)/(\partial \eta)]$ which can be directly written in finite-difference form. Through application of the chain rule and the Cauchy-Riemann relations, it can be shown that

$$Q^2 = \frac{1}{\left(\frac{d\xi}{d\mu}\frac{\partial x}{\partial \xi}\right)^2 + \left(\frac{d\eta}{d\lambda}\frac{\partial x}{\partial \eta}\right)^2} \quad . \tag{3-34}$$

Similarly, the mapping derivatives $(\partial \mu)/(\partial x)$ and $(\partial \lambda)/(\partial x)$ appearing in Equation (3-32) can be expressed in the forms

$$\frac{\partial \mu}{\partial x} = Q^2 \frac{d\xi}{d\mu}\frac{\partial x}{\partial \xi} \tag{3-35}$$

and

$$\frac{\partial \lambda}{\partial x} = Q^2 \frac{d\eta}{d\lambda}\frac{\partial x}{\partial \mu} \quad . \tag{3-36}$$

As shown in Appendix B, the derivatives $(\partial^2 \phi)/(\partial x^2)$, $(\partial^2 \phi)/(\partial y^2)$, and $(\partial^2 \phi)/(\partial x \partial y)$ which appear in the right-hand sides of Equations (3-31) and (3-32) require the calculation of $(\partial^2 \mu)/(\partial x^2)$ and $(\partial^2 \lambda)/(\partial x^2)$. The latter are computed with the following formulas using numerical differentiation:

$$\frac{\partial^2 \mu}{\partial x^2} = \frac{\partial \mu}{\partial x} \frac{d\xi}{d\mu} \frac{\partial}{\partial \xi} \left(\frac{\partial \mu}{\partial x} \right) + \frac{\partial \lambda}{\partial x} \frac{d\eta}{\partial \lambda} \frac{\partial}{\partial \eta} \left(\frac{\partial \mu}{\partial x} \right) \tag{3-37}$$

$$\frac{\partial^2 \lambda}{\partial x^2} = \frac{\partial \mu}{\partial x} \frac{d\xi}{d\mu} \frac{\partial}{\partial \xi} \left(\frac{\partial \lambda}{\partial x} \right) + \frac{\partial \lambda}{\partial x} \frac{d\eta}{d\lambda} \frac{\partial}{\partial \eta} \left(\frac{\partial \lambda}{\partial x} \right) . \tag{3-38}$$

Finally, the cartesian velocity components are computed from the relations

$$u = - Q^2 \frac{d\eta}{d\lambda} \frac{d\xi}{d\mu} \left(\frac{\partial x}{\partial \eta} \frac{\partial \psi}{\partial \xi} - \frac{\partial x}{\partial \xi} \frac{\partial \psi}{\partial \eta} \right) \tag{3-39}$$

$$v = - Q^2 \left[\left(\frac{d\xi}{d\mu} \right)^2 \frac{\partial x}{\partial \xi} \frac{\partial \psi}{\partial \xi} + \left(\frac{d\eta}{d\lambda} \right)^2 \frac{\partial x}{\partial \eta} \frac{\partial \psi}{\partial \eta} \right] . \tag{3-40}$$

3.2 The Finite-Difference Technique

The Poisson equations for stream function and static pressure can be solved numerically without difficulty using the conventional central-difference algorithm. This is not the case for the vorticity transport equation and the Wolfshtein turbulence-model transport equation. The coefficients of the first-order derivatives in these equations contain the Reynolds number as a multiplicative factor, and, as a result, with the standard central-difference algorithm, the discretized system of equations is diagonally dominant for only a limited range in the magnitudes of the coefficients. Diagonal dominance is necessary to obtain convergence in the iterative solution of the discretized system of equations. Details of the finite-difference analysis and the iterative procedure for solving the discretized equations are given.

3.2.1 Discretization of the Governing Equations

The Poisson equation, Equation (3-31), is discretized using the standard central-difference approximations given in Appendix A and the point-of-the compass notation defined in Figure 3.

Poisson equation:

$$A_E\phi_E + A_W\phi_W + A_N\phi_N + A_S\phi_S - A_P\phi_P = B_P, \tag{3-41}$$

where the coefficients are evaluated from the following relations:

$$A_E = \frac{1}{2}\left.\frac{d\xi}{d\mu}\right|_P \left(\left.\frac{d\xi}{d\mu}\right|_E + \left.\frac{d\xi}{d\mu}\right|_P\right) \tag{3-42}$$

$$A_W = \frac{1}{2}\left.\frac{d\xi}{d\mu}\right|_P \left(\left.\frac{d\xi}{d\mu}\right|_P + \left.\frac{d\xi}{d\mu}\right|_W\right) \tag{3-43}$$

$$A_N = \frac{g^2}{2}\left.\frac{d\eta}{d\lambda}\right|_P \left(\left.\frac{d\eta}{d\lambda}\right|_N + \left.\frac{d\eta}{d\lambda}\right|_P\right) \tag{3-44}$$

$$A_S = \frac{g^2}{2}\left.\frac{d\eta}{d\lambda}\right|_P \left(\left.\frac{d\eta}{d\lambda}\right|_P + \left.\frac{d\eta}{d\lambda}\right|_S\right) \tag{3-45}$$

$$A_P = \frac{1}{2}\left.\frac{d\xi}{d\mu}\right|_P \left(\left.\frac{d\xi}{d\mu}\right|_E + 2\left.\frac{d\xi}{d\mu}\right|_P + \left.\frac{d\xi}{d\mu}\right|_W\right)$$

$$+ \frac{g^2}{2}\left.\frac{d\eta}{d\lambda}\right|_P \left(\left.\frac{d\eta}{d\lambda}\right|_N + 2\left.\frac{d\eta}{d\lambda}\right|_P + \left.\frac{d\eta}{d\lambda}\right|_S\right) \tag{3-46}$$

$$B_P = \frac{\sigma_{P,P}a^2}{Q_P^2} \quad . \tag{3-47}$$

Prior to the discretization of the transport equations for vorticity and stream function, Equation (3-32) is rewritten in the form

$$\alpha\frac{\partial^2\phi}{\partial\xi^2} + 2Re\gamma\frac{\partial\phi}{\partial\xi} + \beta\frac{\partial^2\phi}{\partial\eta^2} + 2Re\delta\frac{\partial\phi}{\partial\eta} = Re\sigma_T \ , \tag{3-48}$$

where

$$\alpha = \tau_1 \left(\frac{d\xi}{d\mu}\right)^2 Q^2 \tag{3-49}$$

$$\gamma = \frac{1}{2Re}\left[\tau_1 \frac{d^2\xi}{d\mu^2} Q^2 + \frac{d\xi}{d\mu}\left(\tau_2 \frac{\partial\mu}{\partial x} - \tau_3 \frac{\partial\lambda}{\partial x}\right)\right] \tag{3-50}$$

$$\beta = \tau_1 \left(\frac{d\eta}{d\lambda}\right)^2 Q^2 \tag{3-51}$$

$$\delta = \frac{1}{2Re}\left[\tau_1 \frac{d^2\eta}{d\lambda^2} Q^2 + \frac{d\eta}{d\lambda}\left(\tau_2 \frac{\partial\lambda}{\partial x} + \tau_3 \frac{\partial\mu}{\partial x}\right)\right] . \tag{3-52}$$

In the present work, Equation (3-48) is written in finite-difference form using the augmented-central-difference (ACD) algorithm developed by Hoffman at MDRL[8]. The essence of this method can be illustrated by considering the derivative of $(\partial\phi)/(\partial\xi)$ of Equation (3-48). Using the five-point difference stencil shown in Figure 3 and point-of-the compass notation, this derivative can be evaluated at point P using the following truncated Taylor-series representation and standard central-difference approximation to the first derivative:

$$\left.\frac{\partial\phi}{\partial\xi}\right|_P = \frac{\phi_E - \phi_W}{2a} - \frac{a^2}{6}\left.\frac{\partial^3\phi}{\partial\xi^3}\right|_P - \frac{a^4}{5!}\left.\frac{\partial^5\phi}{\partial\xi^5}\right|_P . \tag{3-53}$$

In the ACD scheme, the derivative $(\partial^3\phi)/(\partial\xi^3)$ is retained and is expressed in terms of lower-order derivatives by differentiating Equation (3-48) with respect to ξ. The derivative $(\partial\phi)/(\partial\eta)$ in Equation (3-48) is represented in an analogous fashion with the ACD algorithm.

With this finite-difference method, Equation (3-48) has the discretized form given below.

Transport equation:

$$C_E\phi_E + C_W\phi_W + C_N\phi_N + C_S\phi_S - C_P\phi_P = D_P \ , \tag{3-54}$$

where the ACD coefficients are defined by the following:

$$C_E = \alpha_P + Re_g\gamma_P + \frac{2Re_g^2\gamma_P^2}{3\alpha_P} \tag{3-55}$$

$$C_W = \alpha_P - Re_g\gamma_P + \frac{2Re_g^2\gamma_P^2}{3\alpha_P} \tag{3-56}$$

$$C_N = \beta_P g^2 + Re_g\delta_P g + \frac{2Re_g^2\delta_P^2}{3\beta_P} \tag{3-57}$$

$$C_S = \beta_P g^2 - Re_g\delta_P g + \frac{2Re_g^2\delta_P^2}{3\beta_P} \tag{3-58}$$

$$C_P = 2\left(\alpha_P + \frac{2Re_g^2\gamma_P^2}{3\alpha_P} + \beta_P g^2 + \frac{2Re_g^2\delta_P^2}{3\beta_P}\right) \tag{3-59}$$

$$D_P = -\frac{2Re_g^2}{3}\left(\gamma_P\theta_1 a^2 + \delta_P\theta_3 \frac{a^2}{g^2}\right) \tag{3-60}$$

$$\theta_1 = \frac{1}{\alpha_P}\left(\frac{\partial\gamma}{\partial\xi}\bigg|_P \frac{\partial\phi}{\partial\xi}\bigg|_P + \frac{\partial\delta}{\partial\xi}\bigg|_P \frac{\partial\phi}{\partial\eta}\bigg|_P + \delta_P \frac{\partial^2\phi}{\partial\xi\partial\eta}\bigg|_P - \frac{1}{2}\frac{\partial\sigma_T}{\partial\xi}\bigg|_P\right) \tag{3-61}$$

$$\theta_3 = \frac{1}{\beta_P}\left(\frac{\partial\gamma}{\partial\eta}\bigg|_P \frac{\partial\phi}{\partial\xi}\bigg|_P + \frac{\partial\delta}{\partial\eta}\bigg|_P \frac{\partial\phi}{\partial\eta}\bigg|_P + \delta_P \frac{\partial^2\phi}{\partial\xi\partial\eta}\bigg|_P - \frac{1}{2}\frac{\partial\sigma_T}{\partial\eta}\bigg|_P\right). \tag{3-62}$$

Boundary conditions are introduced into Equations (3-41) and (3-54) in the following manner: When a Dirichlet condition is specified, the known values of ϕ are imposed on the discretized equations evaluated at the grid line adjacent to the boundary of interest. When a Neumann condition is imposed, the normal derivative is discretized, and the values of ϕ at the grid line adjacent to the boundary outside the solution domain are related to the values of ϕ at the grid line adjacent to the boundary inside the solution domain. The discretized equations evaluated at the boundary points are included in the system of equations to be solved.

The velocity components are computed from Equations (3-39) and (3-40) using conventional central-difference finite-difference approximations.

3.2.2 Solution of the Discretized Equations

The finite-difference equations are solved iteratively using point relaxation with the calculating sequence illustrated in Figure 5. If all the computations were performed with a single computer code, the required computer storage would be excessive. Consequently, three separate codes are used in series.

With the first computer code, the mapping equations are solved interatively for y and x using a relaxation factor of 1.6 until a local maximum residual between successive iterations of 10^{-6} is achieved in the field. The mapping coordinates and derivatives are stored for use by the second computer code.

With the second computer code, the flowfield equations are solved iteratively for the stream function, turbulent kinetic energy, and vorticity using respective relaxation factors of 1.6, 0.8, and 0.8 until maximum local residuals between successive iterations of 10^{-4}, 10^{-3}, and 10^{-4}, respectively,

are achieved. (If a laminar solution is desired, the turbulent viscosity is set to zero everywhere in the field, and the solution of the turbulent-kinetic-energy equation is bypassed in the iteration loop.) The mapping coordinates and derivatives and the stream function, turbulent kinetic energy, and vorticity distributions are stored for use by the third computer code.

With the third computer code, the Poisson equation for static pressure is solved iteratively using a relaxation factor of 1.6 until the maximum residual in the field between successive iterations is 10^{-4}. In the final set of computations, the velocity components are computed.

All computer codes are written in FORTRAN IV for use on the Control Data Corporation CYBER 173 computer of the McDonnell Douglas Automation Company, St. Louis.

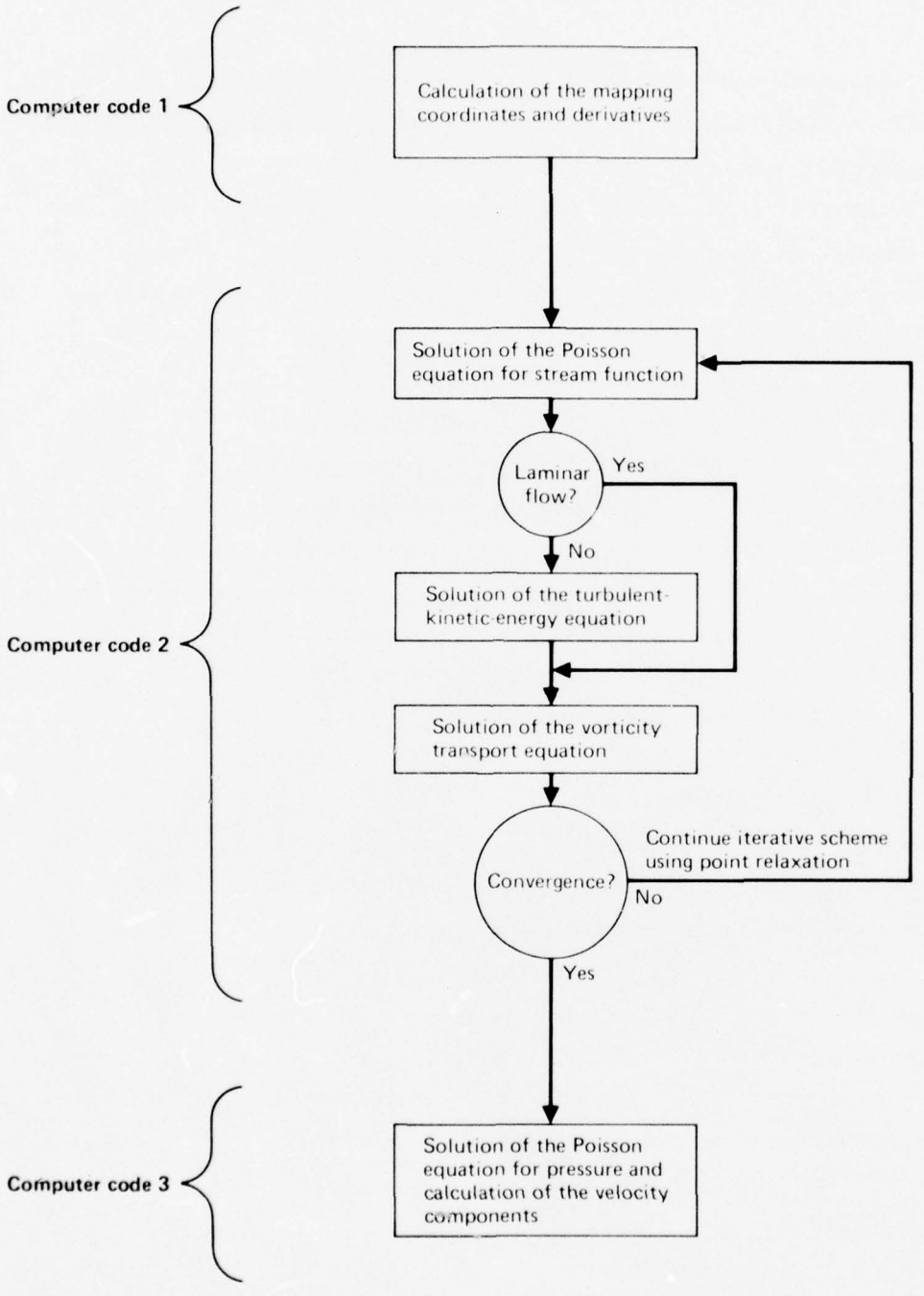

Figure 5 Calculating sequence

4. THE COMPUTED FLOWFIELD SOLUTIONS

In the present work, flowfield solutions have been carried out for three geometric variations of the planar impinging jet shown in Figure 1. The first geometry is a free-upper-boundary configuration, so called because the upper boundary of the solution domain is several diameters below the slot from which the jet discharges. This configuration was selected since it has been analyzed by Wolfshtein[7] and offers a means of comparing the MDRL solutions. The second geometry is a parallel-plate configuration in which the jet discharges from a slot in the upper surface and impinges perpendicular to the lower surface. This configuration was included in the study since it offers a means of evaluating the flowfield model and solution scheme without the added numerical complexity of conformal mapping. The third geometry is the configuration of primary interest in which the jet issues from a curved plate that simulates a fuselage undersurface. Both an unvectored and a vectored jet are considered, and in the former case solutions are presented for two jet-height-above-ground spacings and for two Reynolds numbers with one of the H values.

4.1 The Free-Upper-Boundary Geometry

The free-upper-boundary geometry is illustrated in Figure 6. A free, turbulent, symmetric plane jet issues vertically downward onto the ground plane. Since the problem is geometrically symmetric with respect to the centerline of the jet, only half of the flow domain need be solved. The vorticity and stream function are antisymmetric about the centerline, and the turbulent kinetic energy is symmetric. Thus, the solution domain extends a distance H above the ground plane and a distance W to the right of the line of geometric symmetry. No conformal mapping is required since the boundaries are rectangular, and coordinate stretching is not used. These simplfications result in $x = \xi$ and $y = \eta$.

The imposed boundary conditions are shown in Figure 6. On the upper boundary of the solution domain within the jet, the imposed velocity profile determines the stream function and vorticity distributions, and the turbulent-kinetic-energy profile is specified. Outside the jet, along the remainder of the upper boundary, the flow is taken to be irrotational and normal to the free surface with no turbulent fluctuations. The boundary conditions on

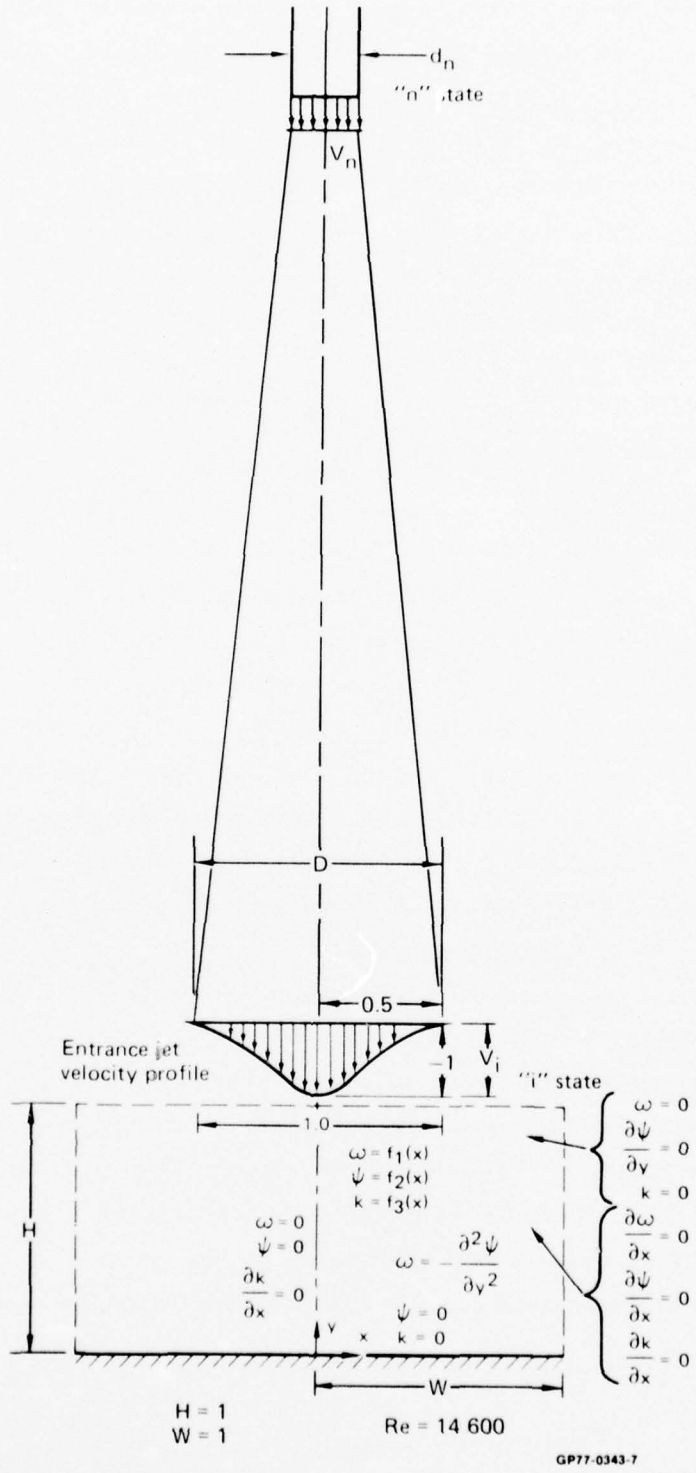

Figure 6 Free-upper-boundary geometry

the jet centerline result from symmetry; on the lower surface they result from the no-slip, impermeable wall constraint. The flow at the right boundary is taken to exit parallel to the wall with no gradients of turbulent kinetic energy in the mainstream direction. The dimensionless length scale variations used are those proposed by Wolfshtein[7].

$$\ell_\mu = y \left[1 - \exp\left(-\mathrm{Re}A_\mu k^{1/2} y\right)\right] \tag{4-1}$$

$$\ell_D = y \left[1 - \exp\left(-\mathrm{Re}A_D k^{1/2} y\right)\right] \quad , \tag{4-2}$$

where A_μ and A_D are empirically determined constants with values of 0.016 and 0.21, respectively. Following Wolfshtein, if the magnitudes of the length scales exceed 0.1, ℓ_μ and ℓ_D are set to 0.1.

The flow variables were computed with H = 1, W = 1, and a Reynolds number of 14 600 based on jet properties at the upper boundary of the solution domain (denoted "i" state in Figure 6), which corresponds to a Reynolds number of 11 000 based on properties at the nozzle exit plane (denoted "n" state in Figure 6). Computations were performed using a 41 x 41 uniform finite-difference grid.

Contour plots of the normalized primary flow variables are given in Figure 7. The vorticity distribution shows the convection of ω to the right and the development of the lower wall boundary layer, and the stream function plot illustrates the entrainment of fluid into the free jet. The distribution of turbulent-kinetic-energy, which has a peak value of 0.04 imposed at the upper boundary within the jet, shows the convection of k toward the right boundary and a plateau of maximum k in the vicinity of the stagnation point, indicating a rate of high turbulence generation in this region.

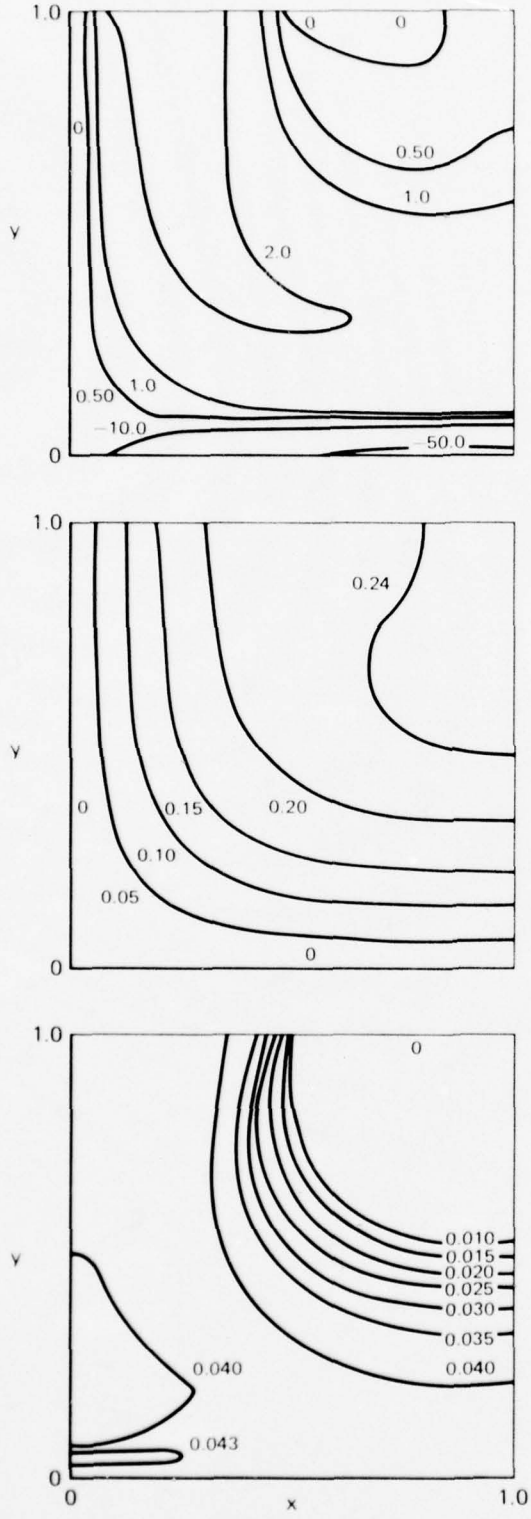

Figure 7 Primary flow variables for the free-upper-boundary geometry (H = 1, W = 1, Re = 14 600)

GP77-0343-8

The normalized primitive flow variables are shown in Figure 8. The contour plot of the x component of velocity clearly shows the development of the wall boundary layer and the entrainment of fluid into the jet, and the plot of the y component of velocity depicts the decay in v as the stagnation point is approached. The variation of static pressure shows a small normal pressure gradient through the wall boundary layer and a generally favorable pressure gradient along the wall as the flow accelerates to the right.

The free-upper-boundary geometry defined in Figure 6 has been analyzed by Wolfshtein[7] for the case of laminar flow with the results presented in Reference 9. A comparison of the MDRL laminar-flow solutions with those of Wolfshtein for H = W = 1 and Reynolds numbers of 1 and 1000 is given in Figure 9. Wolfshtein's turbulent-flow solutions are not for a solution domain with H = W = 1, so the corresponding comparison for the case of turbulent flow is not applicable.

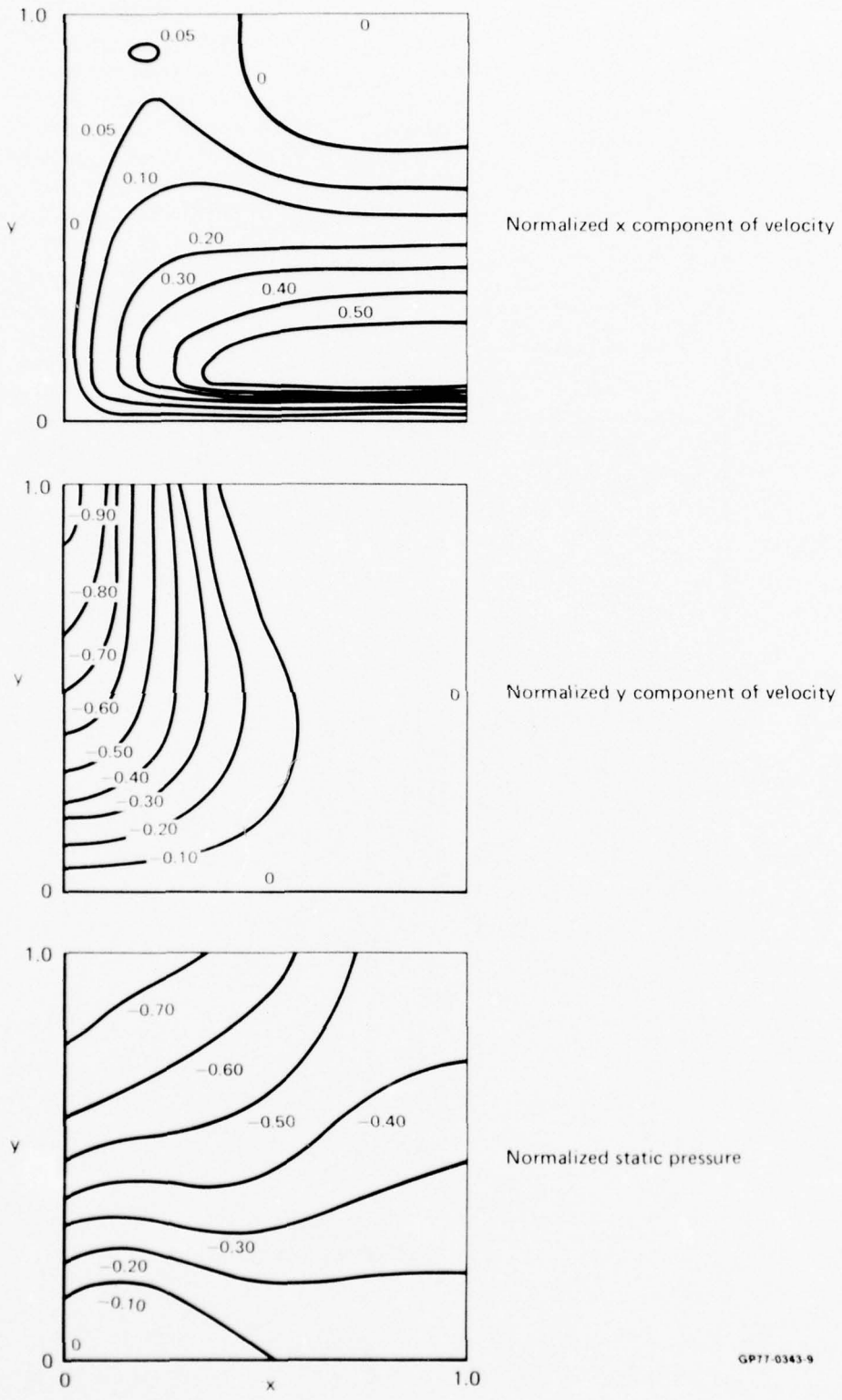

Figure 8 Primitive flow variables for the free-upper-boundary geometry (H = 1, W = 1, Re = 14 600)

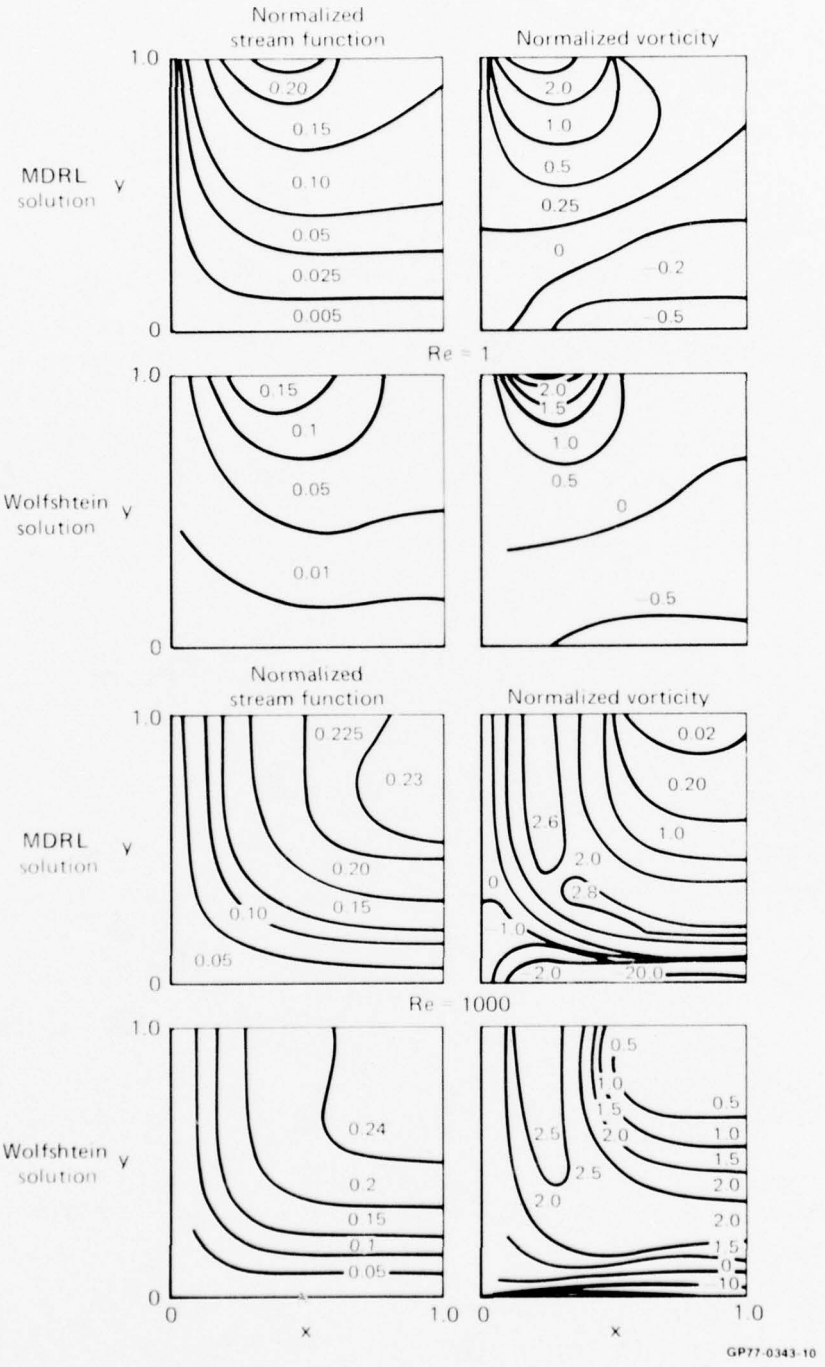

Figure 9 Comparison of MDRL laminar-flow solutions with those of Wolfshtein[7,9]

4.2 The Parallel-Plate Geometry

The parallel-plate geometry is shown in Figure 10. A turbulent, symmetric plane jet discharges from a slot in the upper flat plate and impinges normal to the ground plane a distance H below. As in the free-upper-boundary case, the flow is solved only for the half plane (extending a distance W to the right of the jet centerline) to take advantage of geometric symmetry. Again, no conformal mapping is needed since the boundaries are rectangular, and coordinate stretching is not used; thus, $x = \xi$ and $y = \eta$.

The boundary conditions for this geometry are illustrated in Figure 10(a). The values of vorticity, stream function, and turbulent kinetic energy are specified within the entering jet, and along the upper wall they result from the no-slip, impermeable wall constraint. The conditions imposed on the remaining three boundaries are identical to those used for free-upper-boundary geometry.

For the parallel-plate configuration, the accuracy of the assumption of no gradients in the flow properties at the right boundary deteriorates as the ratio H/W of the solution domain is increased. A more general right-boundary condition is one in which a normal-pressure-gradient profile and a turbulent-kinetic-energy profile are imposed. The corresponding vorticity and stream function distributions must then be computed iteratively from the Poisson equation for stream function and the y-momentum equation, where $(\partial p)/(\partial y)$ is known. However, presently the required experimental pressure-gradient and turbulent-kinetic-energy distributions are not known for the configuration of interest, and the assumption of parallel flow is invoked.

For the parallel-plate geometry, actual length-scale distributions are similarly unknown. Consequently, the following constraints based on simple order-of-magnitude arguments have been used to suggest physically realistic distributions of $\ell_\mu = \ell_D = \ell$: at a wall, $\ell = 0$; at $y = H/2$, $\ell = H/2$ and $(d\ell)/(dy) = 0$; and within the region of the entering jet given by $(0 \le x \le 0.25,\ y = H)$, $\ell = 0.5$. These conditions are satisfied by the following polynomials:

$$\ell = \ell_1 = 2\left(\frac{y}{H}\right)\left[\left(\frac{y}{H}\right)^2 - (H+1)\left(\frac{y}{H}\right) + \frac{1}{4}(1+4H)\right] \qquad (4\text{-}3)$$

$$0 \le x \le 0.25$$

and

$$\ell = \ell_2 = 2y\left(1 - \frac{y}{H}\right) \qquad 0.5 \le x \le W. \tag{4-4}$$

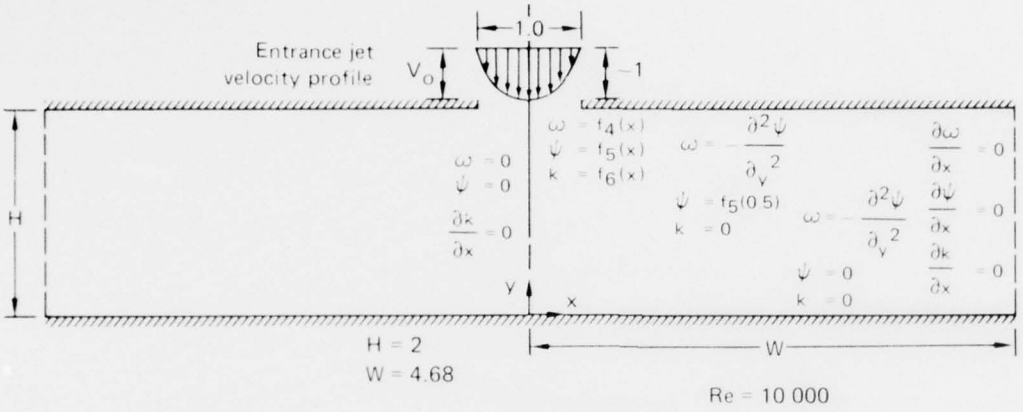

(a) Specification of boundary and flow conditions

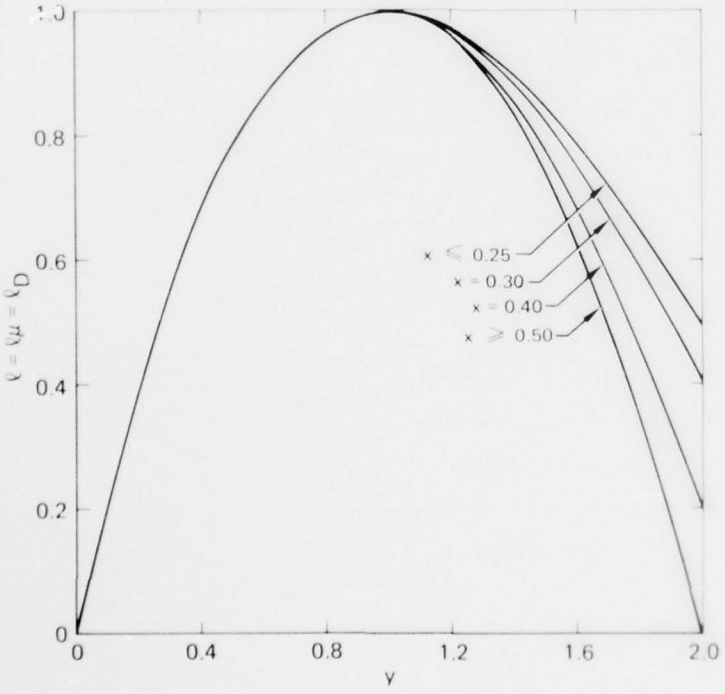

(b) Length-scale distribution as a function of y for the parallel-plate geometry with H = 2

GP77-0343-11

Figure 10 Parallel-plate geometry

In the region $0.25 < x < 0.5$, the following combination of ℓ_1 and ℓ_2 is used to represent ℓ:

$$\ell = 4 \left[(0.5 - x)\, \ell_1 + (x - 0.25)\, \ell_2 \right] \qquad 0.25 < x < 0.5. \tag{4-5}$$

Equations (4-3) through (4-5) are entirely geometric functions and, unlike Equations (4-1) and (4-2), do not contain exponential terms that depend on the turbulent kinetic energy, Reynolds number, and empirical constants. Figure 10(b) illustrates the length-scale distributions for a parallel-plate geometry with H = 2.

Calculations were made with H = 2, W = 4.68, and a Reynolds number of 10 000 based on properties at the jet exit slot.

Figure 11 shows the computed primary flow variables. Vorticity is convected to the right boundary of the solution domain with development of an attached boundary layer on the lower surface and a separated boundary layer on the upper surface. (Separation occurs on a solid boundary where $\omega = 0$, and in the present configuration this occurs very near the slot edge.) The region of recirculating flow is clearly illustrated by the stream function plot. The maximum value of turbulent kinetic energy imposed on the entering jet is 0.04, and as the contour plot of k reveals, there is a decay from this value throughout the field. Over the right half of the solution domain, the turbulent kinetic energy is fairly uniform.

The primitive flow variables are given in Figure 12. The contour plots of the two velocity components define in more detail the region of recirculation between the plates. The distribution of the x component of velocity illustrates the upper- and lower-wall boundary layers and the entrainment of fluid into the jet. The sharp pressure gradient in the impingement region is shown in the plot of the static pressure, where the value of pressure at the stagnation point has been set equal to one.

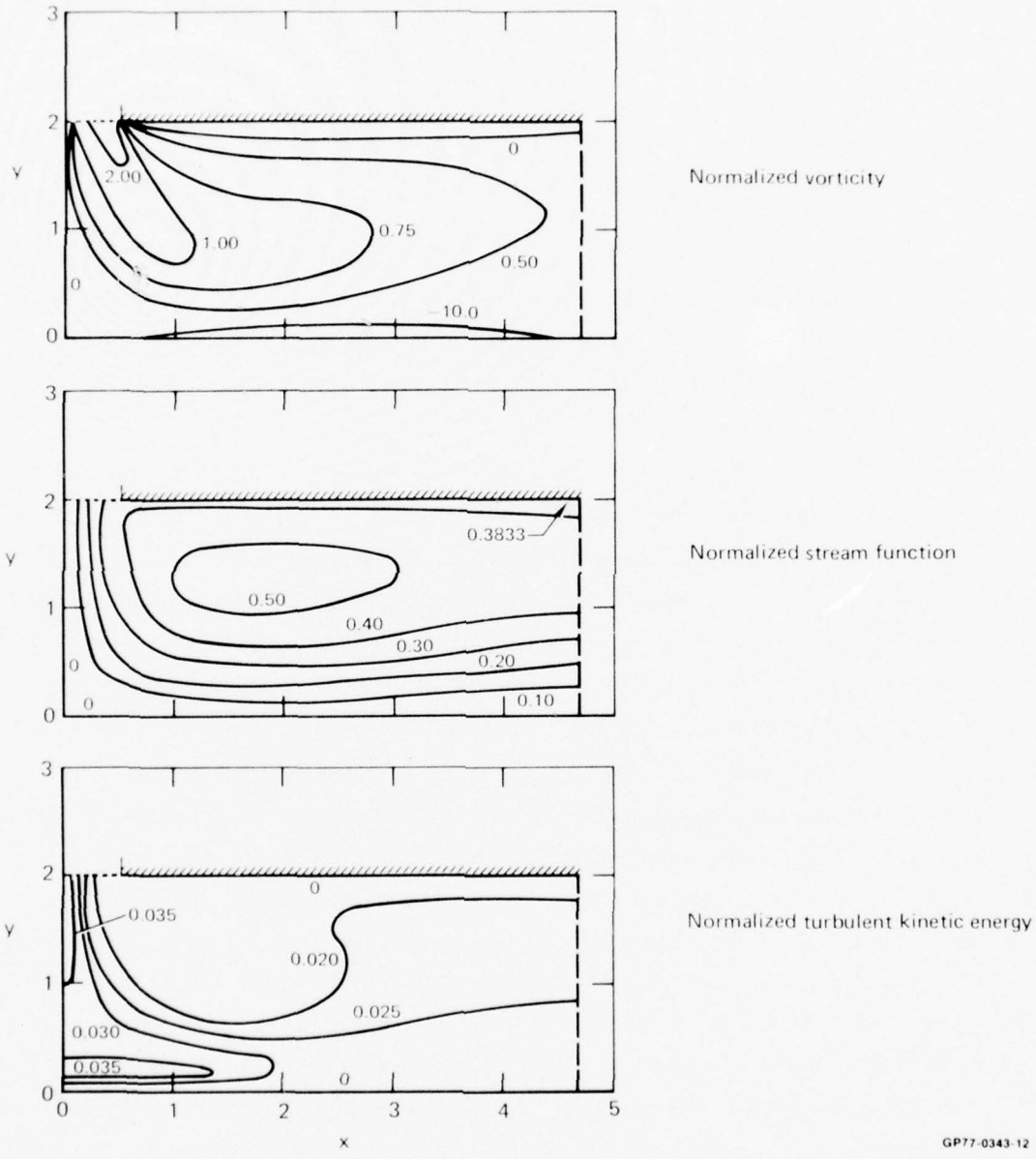

Figure 11 Primary flow variables for the parallel-plate geometry (H = 2, W = 4.68, Re = 10 000)

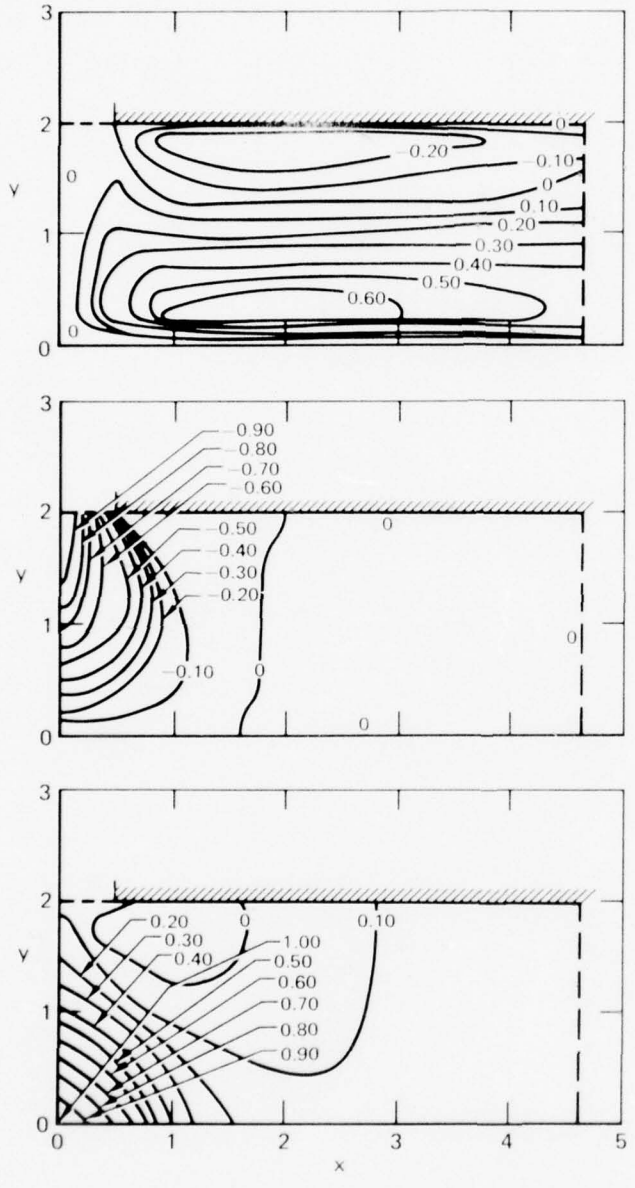

Figure 12 Primitive flow variables for the parallel-plate geometry (H = 2, W = 4.68, Re = 10 000)

4.3 The Curved-Plate Geometry

A jet discharging from a curved upper surface and striking a ground plane is the geometry of major interest in the present study since this configuration best simulates, in a two-dimensional sense, a lift-jet issuing from a simulated fuselage undersurface in ground effect. Figure 13 illustrates the curved-plate geometry for which vectored and unvectored jet impingement flowfields are being measured in a MDRL IRAD test series and which have been computed in the present contract work.

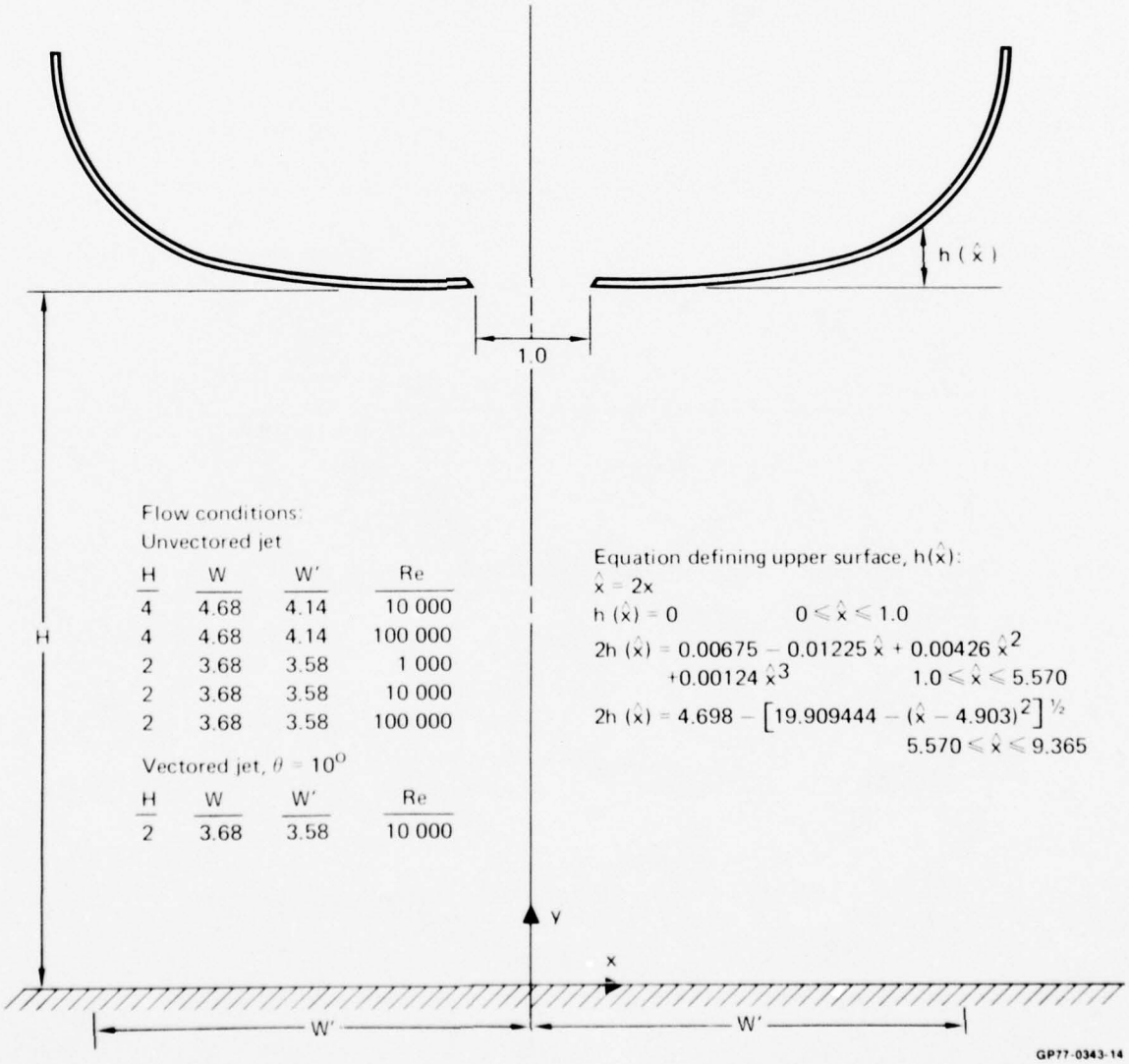

Figure 13 Definition of curved-plate geometry and specification of flow conditions

The conformal mapping scheme described in Section 3.1, without the use of stretching functions, was applied to this geometry, and solutions were carried out for the flow conditions specified in Figure 13.

In all cases, the mapping equations were solved for only the half-plane; to treat the complete flowfield for the vectored jet, the required mapping derivatives were reflected about the line of geometric symmetry. With regard to the half-plane, W denotes the width of the computational plane, and W' denotes the half-width of the upper boundary of the physical plane. The half-width of the model, normalized by the jet slot width, is 4.68, but a convergent solution of the mapping equations could not be achieved when W' was extended to this value. The mapping procedure requires that body slopes be finite, but for the curved-plate geometry, $(dy)/(dx)$ is extremely large in the vicinity of $x = 4.68$. The largest value of W' for which a convergent solution could be obtained decreased as H was reduced. For this reason, the values of W' specified in Figure 13 are not equivalent to the half-width of the curved-plate geometry.

The boundary conditions in the computational plane imposed on the flowfield solution for the curved-plate geometry are shown in Figure 14.

Consider first the boundary conditions for the unvectored jet, Figure 14(b). Only the right half of the flowfield is solved since the problem is again geometrically symmetric with respect to the jet centerline. The vorticity, stream function, and turbulent-kinetic-energy profiles are specified within the entering jet. On the upper and lower surfaces, the boundary conditions result from the constraint of a no-slip, impermeable wall. On the jet centerline the symmetry conditions are imposed, and at the right boundary the flow properties are taken to be uniform with respect to ξ. It is recognized that this condition becomes increasingly inaccurate with decreasing W, and in future work experimentally obtained flow quantities can be imposed.

Consider now the boundary conditions used with the vectored jet, Figure 14(c). In this configuration the solution must be carried out for the entire flowfield with a width 2W in the computational plane. Within the entering jet, the vorticity and stream function variations are computed from the velocity profile obtained by rotating the profile imposed in the unvectored case through an angle θ with respect to the line of geometric symmetry. The turbulent-kinetic-energy distribution is

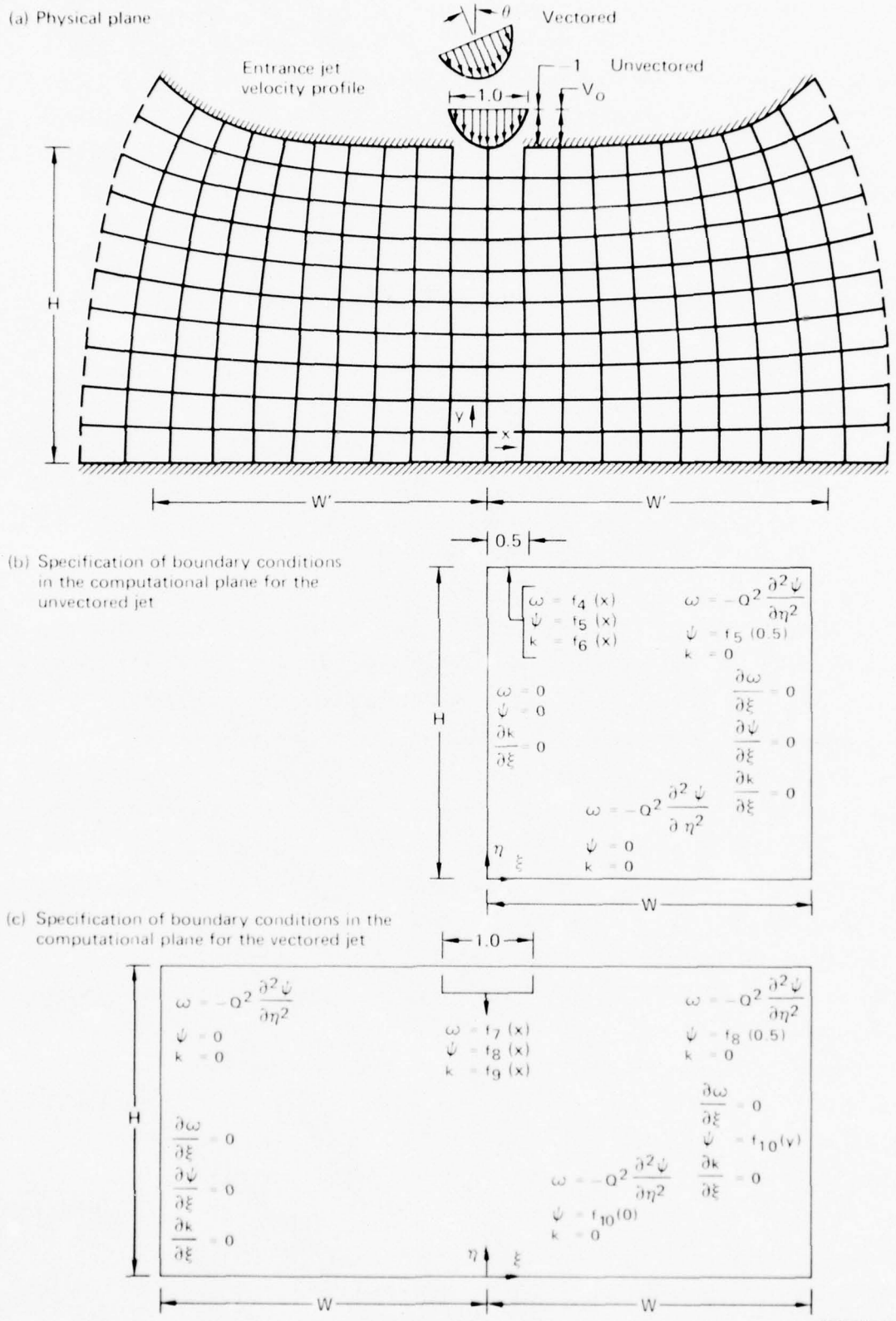

Figure 14 Curved-plate geometry

also obtained through an axis rotation of the unvectored k distribution. Values of ω, ψ, and k on the solid surfaces are evaluated from the no-slip, impermeable wall condition. The constraints given by $(\partial\omega)/(\partial\xi) = (\partial k)/(\partial\xi) = 0$ are imposed on both the right and left boundaries of the solution domain; however, the condition $(\partial\psi)/(\partial\xi) = 0$ is applied only at the left boundary, and a ψ distribution (obtained through integration of a specified u profile), is imposed on the right boundary. This is necessary to evaluate the lower-wall stream function since ψ can no longer be integrated along the jet centerline from the upper boundary to the lower boundary, as is done in the unvectored case.

The length-scale distributions used are those given by Equations (4-3) through (4-5) with H replaced by y_{max}, the coordinate of the upper surface.

For the unvectored configuration, 41 grid points were used in both the ξ and η directions in the finite-difference solution. For the vectored configuration, 41 grid points were used in the ξ direction and 21 in the η direction.

4.3.1 The Unvectored Jet

Primary and primitive flow variables computed for the curved-plate geometry with H = 4, W = 4.68, and Re = 10 000 are shown in Figures 15 and 16, respectively, for the case of normal jet impingement. The flow profiles are qualitatively similar to those presented for the parallel-plate geometry. However, in the curved-plate configuration, with the larger aspect ratio of the solution domain (H/W), the region of recirculating flow does not lie completely within the confining boundaries.

Solutions were computed for the configuration with Re = 100 000, but they are indistinguishable from those computed for Re = 10 000. The reason is apparent from Equation (2-39); for large Reynolds numbers, the normalized molecular viscosity (1/Re) is a very small contribution to the effective viscosity. The latter is dominated by the turbulent contribution, which is controlled by the specified geometric length scales and not by the Reynolds number based on the molecular viscosity.

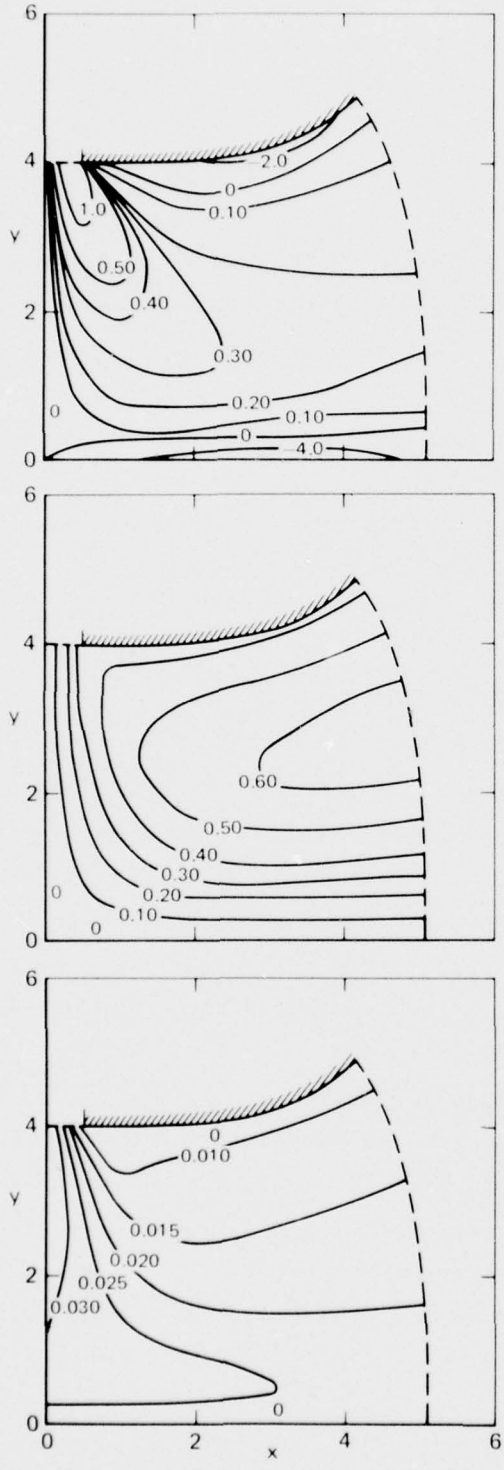

Normalized vorticity

Normalized stream function

Normalized turbulent kinetic energy

GP77-0343-16

Figure 15 Primary flow variables for the curved-plate geometry (H = 4, W = 4.68, Re = 10 000)

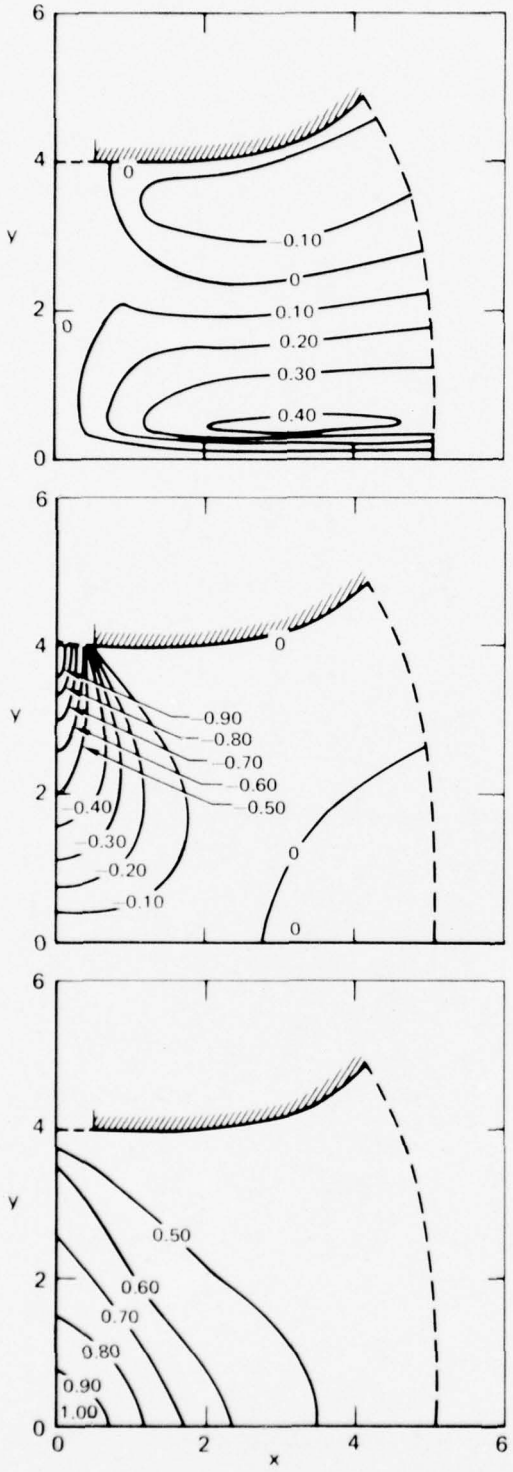

GP77-0343-17

Figure 16 Primitive flow variables for the curved-plate geometry (H = 4, W = 4.68, Re = 10 000)

Primary and primitive flow variables computed for the curved-plate geometry with H = 2 and W = 3.68 are shown in Figures 17 and 18 for Re = 1000 and in Figures 19 and 20 for Re = 10 000. Solutions carried out with Re = 100 000 are indistinguishable from the latter and are not shown.

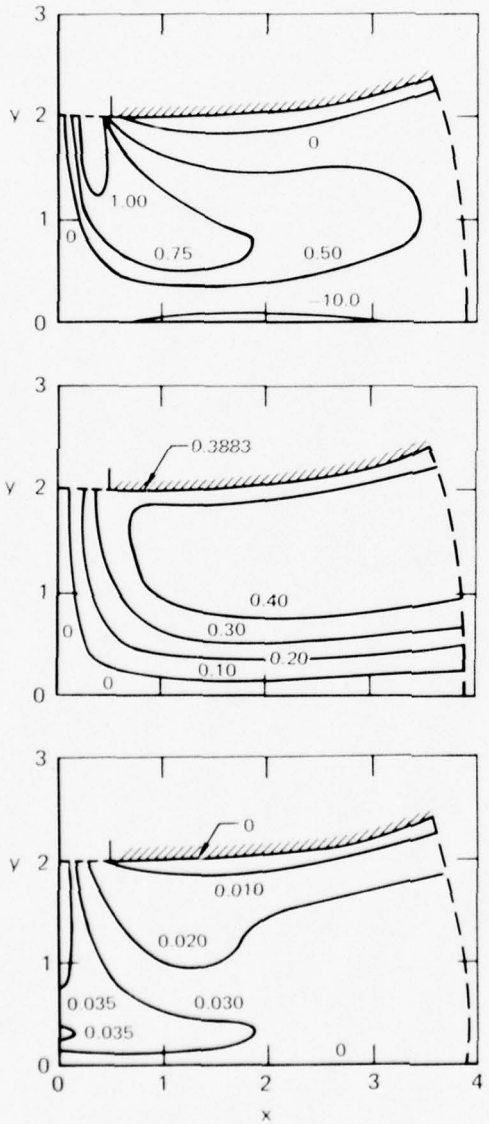

Normalized vorticity

Normalized stream function

Normalized turbulent kinetic energy

GP77-0343-18

Figure 17 Primary flow variables for the curved-plate geometry (H = 2, W = 3.68, Re = 1000)

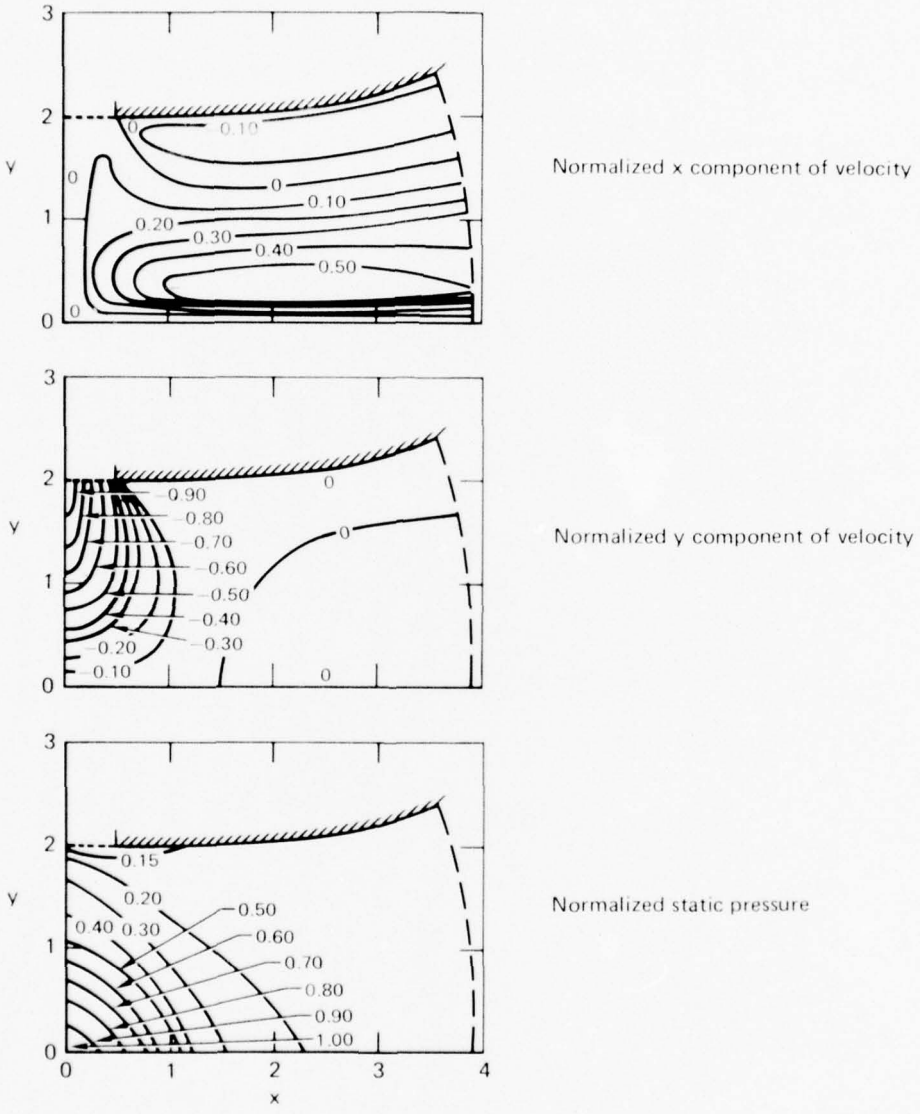

Figure 18 Primitive flow variables for the curved-plate geometry (H = 2, W = 3.68, Re = 1000)

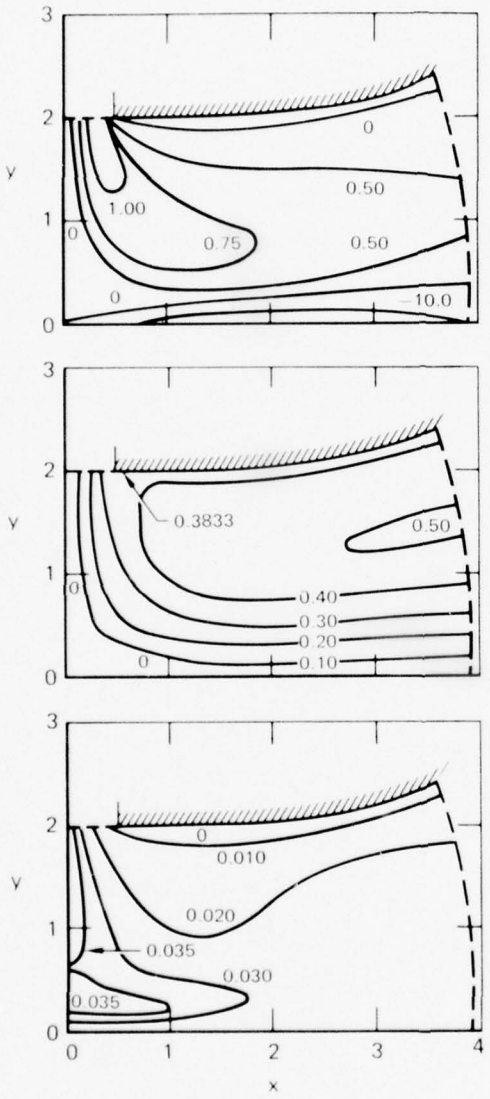

Normalized vorticity

Normalized stream function

Normalized turbulent kinetic energy

GP77-0343-20

Figure 19 Primary flow variables for the curved-plate geometry (H = 2, W = 3.68, Re = 10 000)

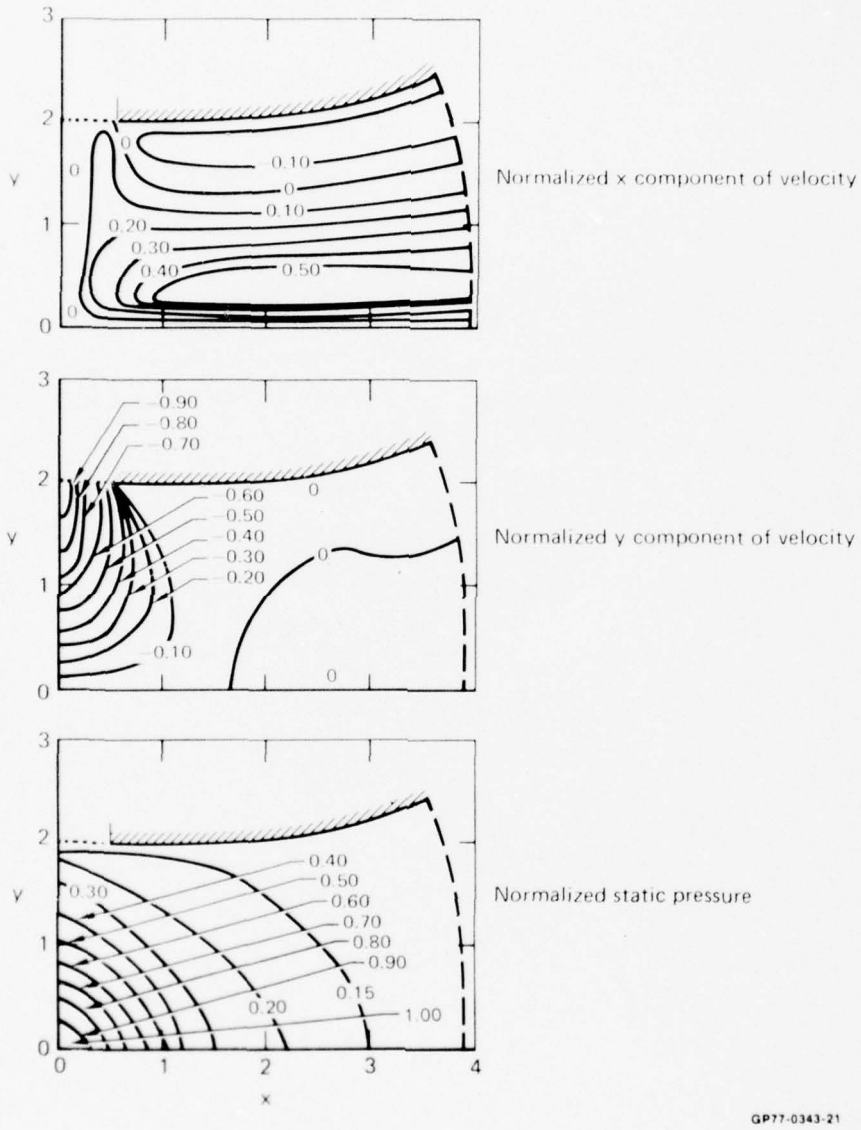

Figure 20 Primitive flow variables for the curved-plate geometry (H = 2, W = 3.68, Re = 10 000)

Differences between the computed flow properties for the case with Re = 1000 and Re = 10 000 are relatively small for the reason cited previously. The level of turbulence generation near the stagnation point increases with Reynolds number, as illustrated by the plots of turbulent kinetic energy. However, there is no significant variation in the entrainment level for a change in Re from 1000 to 10 000.

In comparing the curved-plate flowfield solution for H = 2 with that for H = 4 at a Reynolds number of 10 000, there is a more accelerated movement of the flow toward the right boundary in the first case.

Figure 21 present various static pressure and velocity profiles for the curved-plate configuration with H = 2, W = 3.68, and Re = 10 000. The static pressure distributions for the upper and lower surfaces give the expected trends, most notably the large drop in the lower wall pressure within the impingement region. The plot of jet centerline static pressure and velocity shows the rapid decay of the jet potential core. The distributions of the normalized x component of velocity at various x stations display the characteristic wall jet profiles; clearly, there is an extensive region of flow reversal.

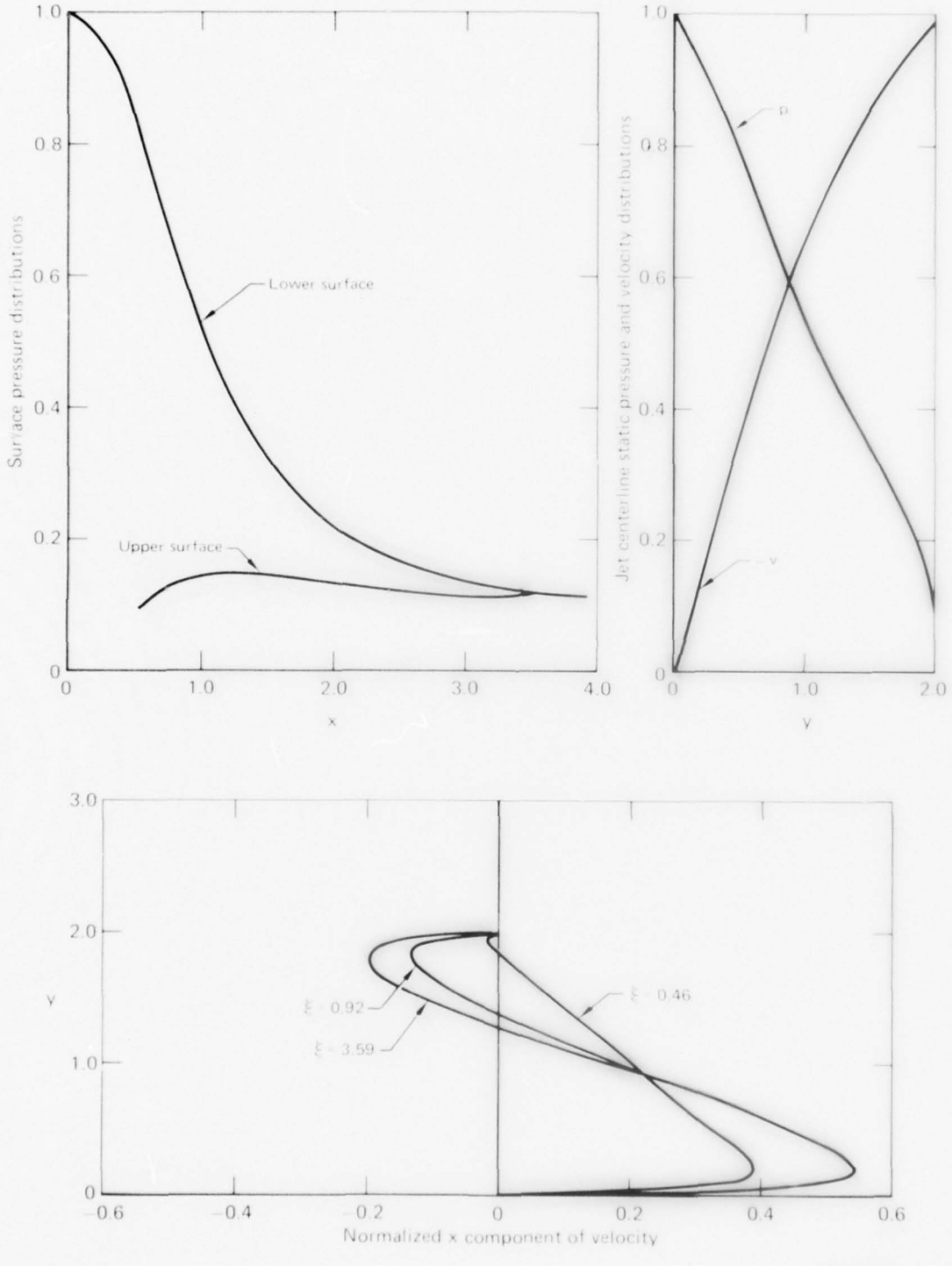

Figure 21 Flow profiles for the curved-plate geometry (H = 2, W = 3.68, Re = 10 000)

4.3.2 The Vectored Jet

As an initial test case for the computer code used to compute the vectored jet flowfield, a solution was carried out for an unvectored configuration to verify that in the limiting case of $\theta = 0°$ the correct flow pattern is obtained. Figure 22 presents the primary flow variables for the complete curved-plate geometry with H = 2, W = 3.68, and Re = 10 000. Since the value of the lower-surface stream function can be set to zero in this case, the problem was solved subject to Neumann boundary conditions on all three primary flow variables at both the left and right boundaries. That is, for the unvectored jet the right boundary condition $\psi = f_{10}(y)$ specified in Figure 14(c) was replaced by $(\partial\psi)/(\partial\xi) = 0$, and the lower boundary condition $\psi = f_{10}(0)$ was replaced by $\psi = 0$. Figure 22 clearly illustrates the asymmetry of the vorticity and stream function distributions and the symmetry of the turbulent-kinetic-energy distribution. The differences between the curved-plate flowfields computed for the full plane (Figure 22) and the half plane (Figure 17) are attributed to the differences in the finite-difference mesh sizes used. The former were calculated with a coarser mesh to conserve machine computing time.

A solution was also carried out for the complete curved-plate geometry with H = 2, W = 3.68, $\theta = 10°$, and Re = 10 000. In this vectored jet geometry, the value of the stream function on the lower surface is not known a priori unless a simple horizontal momentum balance is applied assuming inviscid impingement flow. In lieu of this assumption, the boundary condition imposed at the right boundary was evaluated from the x-component-of-velocity computed for the unvectored jet with the same velocity profile. The resulting solution was an unrealistic flow pattern, which indicates that physically correct conditions must be imposed at the flowfield boundaries. Work is continuing on the solution of this flowfield.

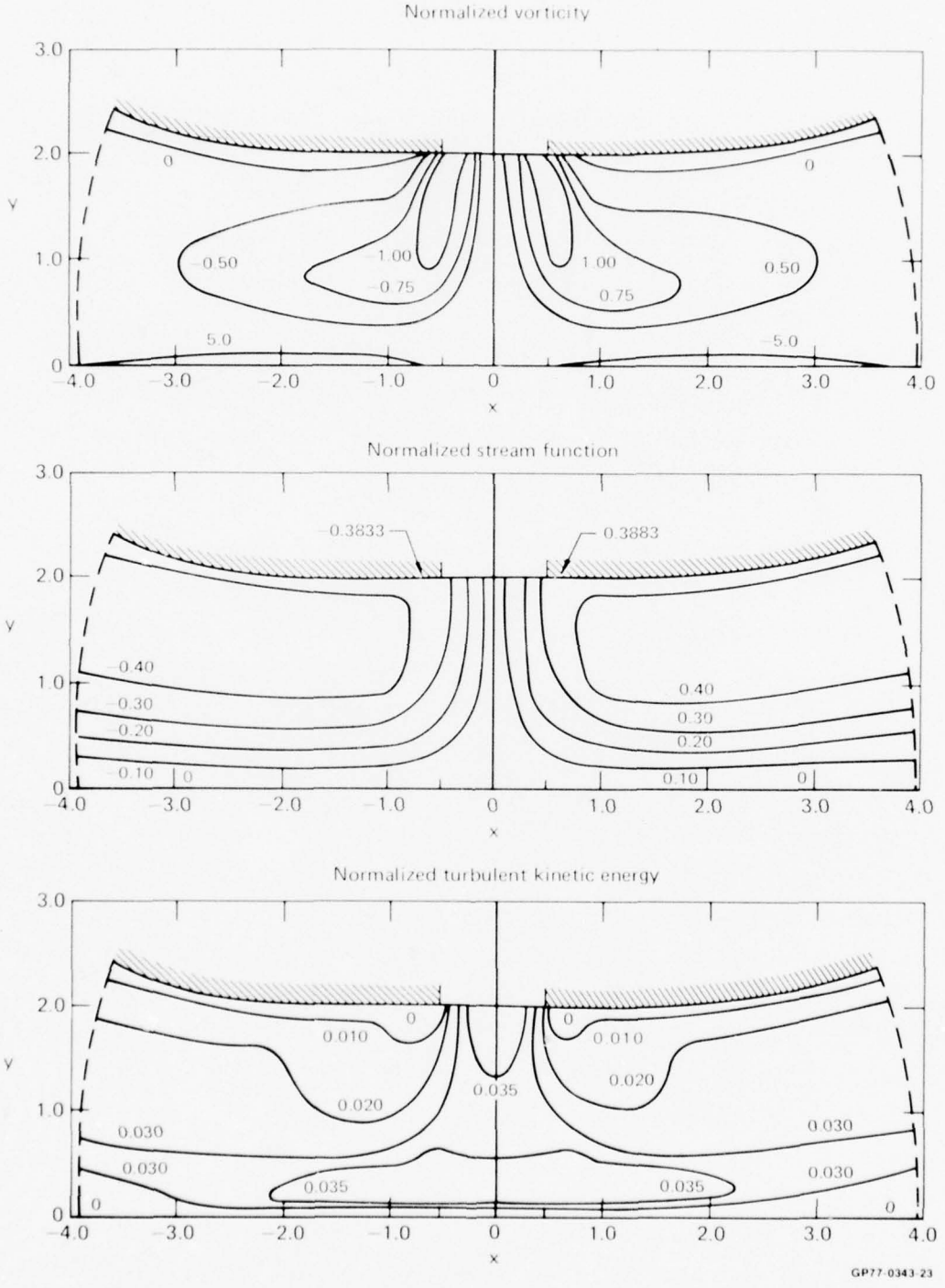

Figure 22 Primary flow variables for the complete curved-plate geometry with an unvectored jet (H = 2, W = 3.68, Re = 10 000)

5. SUMMARY

Starting with the complete elliptic conservation equations for incompressible, steady, viscous flow, an analytical flowfield model for a single two-dimensional (planar) lift jet in ground effect has been formulated and solved numerically. The governing equations are the Reynolds equations and a turbulence model equation which are cast in terms of two transport equations (one for vorticity and one for turbulent kinetic energy) and two Poisson equations (one for stream function and one for static pressure). The latter are solved using finite-difference procedures in conjunction with a conformal mapping technique to treat solution domains with non-rectangular upper boundaries. Flowfields have been computed for three geometries with various jet impingement configurations and Reynolds numbers.

5.1 Conclusions

With regard to the numerical scheme, no significant problems have been encountered in solving the coupled system of equations describing the time-averaged flowfield for the unvectored lift jet. For the vectored configuration, a better definition of the right-boundary conditions is required to obtain a physically realistic representation of the flowfield. Convergent solutions of the conformal mapping equations without the use of coordinate stretching have been obtained for a contoured upper surface except when that surface contains a region of very large slope.

With regard to the analytical model, the computed solutions display all the expected characteristics of a jet impingement flowfield: the lower-surface boundary layer with the typical wall-jet velocity profile, the upper-surface boundary layer with separation, the considerable pressure gradients and high level of turbulent fluctuations in the impingement region, and the distribution of velocity along the jet centerline. These flow patterns are based on postulated boundary conditions at the jet entrance and exit planes and on postulated length-scale distributions. These were derived using order-of-magnitude arguments obtained from simple physical reasoning, since the experimental data required for a more precise definition were not available.

The accuracy of the assumed boundary conditions and length-scale distributions will be established through a comparison of the theoretical flowfields with data obtained in an MDRL IRAD test program. The latter is devoted to the measurement of planar jet impingement flowfields in close ground effect for the flat-plate and curved-plate geometries considered in the present contract work.

5.2 Recommendations

Following a detailed comparison of the computed and measured flow properties, the boundary and length-scale distributions should be improved as necessary to provide a more precise model of the flow. If a simple parametric study cannot be used to provide improved length-scale variations, a two-equation model of turbulence is proposed to compute more accurate length scales. The latter would then be used in the one-equation-model, eliminating the additional machine computation time required to perform the calculations with a two-equation formulation of the turbulence field. Using the improved length scales, the flowfield solutions for the configuration of primary interest, the curved-plate geometry, should be carried out for ranges in values of Re and H in order to establish the influence of the latter on the turbulent entrainment and the surface static pressure distributions.

With the completion of this effort for the case of incompressible flow, it is proposed that the analysis be extended to the case of compressible flow for the same configurations. Such an extension is justified since in reality the fluid in the lift jet is at a temperature much higher than that of the surrounding fluid, and the immediate flowfield has large density gradients. For a VTOL aircraft in ground effect, this can be significant as a result of one or more of the following mechanisms:

(1) Density variations between the ambient air and the less dense lift lift jet have an influence on the entrainment of air at the free boundaries of the free jet and the ground wall jets.

(2) Mixing of the ambient entrained air with the hot lift jet fluid thickens the free jet and the wall jet and leads to a decay in the maximum temperature and velocity with distance from the lift jet exit. The heated wall jet will eventually separate from the ground because of buoyant forces.

(3) Impingement of the hot free jet can appreciably heat the ground surface.

A solution of the compressible Reynolds equations in conjunction with an appropriate turbulence model and thermal energy equation could be used to gain a fundamental understanding of these phenomena. The results of such an analysis would be velocity, pressure, density, and temperature distributions as functions of the significant dimensionless parameters.

REFERENCES

1. I. Tani and Y. Komatsu, Proceedings of the Eleventh International Congress of Applied Mechanics, 1966, pp. 672-676.
2. C. du P. Donaldson and R. S. Snedeker, A Study of Free Jet Impingement. Part 1. Mean Properties of Free and Impinging Jets, Journal of Fluid Mechanics, 45, 281 (1971).
3. L. Gray and E. Kisielowski, Practical Engineering Methods for Predicting Hot Gas Jet-Lift Engines, NASA CR 111845, February 1971.
4. L. J. S. Bradbury, The Impact of an Axisymmetric Jet onto a Normal Ground, Aeronautical Quarterly, 23, 141 (1972).
5. W. C. Reynolds, Computation of Turbulent Flows, Annual Review of Fluid Mechanics, (Annual Reviews Inc., Palo Alto, 1976), Vol. 8, pp. 183-208.
6. T. Cebeci and A. M. O. Smith, Analysis of Turbulent Boundary Layers, (Academic Press, New York, 1974).
7. M. Wolfshtein, Convection Processes in Turbulent Impinging Jets, Report SF/R/2, Department of Mechanical Engineering, Imperial College of Science and Technology, November 1967.
8. G. H. Hoffman, Calculation of Separated Flows in Internal Passages, Proceedings of a Workshop on Prediction Methods for Jet V/STOL Propulsion Aerodynamics, M. F. Platzer, Ed. (Naval Air Systems Command Research and Technology Group, 1975), Vol. 1, pp. 114-124.
9. A. D. Gosman, W. M. Pun, A. K. Runchal, D. B. Spalding, and M. Wolfshtein, Heat and Mass Transfer in Recirculating Flows, (Academic Press, New York, 1969).

APPENDIX A: CENTRAL-DIFFERENCE APPROXIMATIONS FOR THE DERIVATIVES

The second-order-accurate, central-difference approximations used in the discretization of the differential equations are given in this appendix. The finite-difference formulas, written for a general variable ϕ, are expressed in terms of point-of-the-compass notation defined in Figure A-1 for both interior and boundary points.

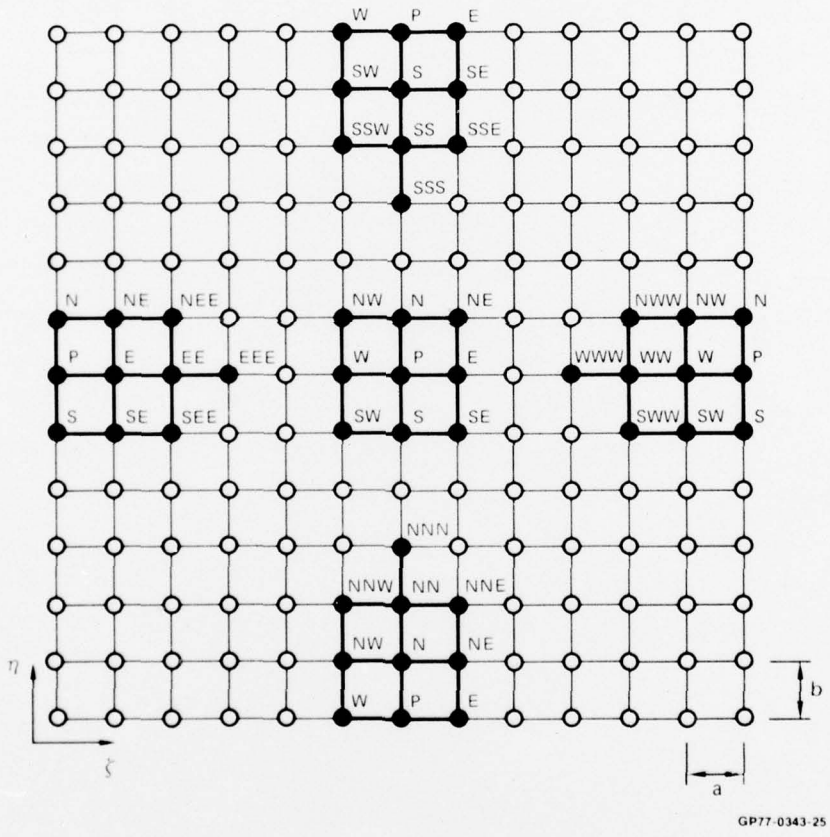

GP77-0343-25

Figure A-1 Grid notation used in the central-difference approximation for the derivatives

$\frac{\partial \phi}{\partial \xi}$ for interior points and for upper- and lower-boundary points:

$$\left.\frac{\partial \phi}{\partial \xi}\right|_P = \frac{\phi_E - \phi_W}{2a} \quad . \tag{A-1}$$

$\frac{\partial \phi}{\partial \xi}$ for left-boundary points:

$$\left.\frac{\partial \phi}{\partial \xi}\right|_P = \frac{4\phi_E - \phi_{EE} - 3\phi_P}{2a} \quad . \tag{A-2}$$

$\frac{\partial \phi}{\partial \xi}$ for right-boundary points:

$$\left.\frac{\partial \phi}{\partial \xi}\right|_P = \frac{\phi_{WW} + 3\phi_P - 4\phi_W}{2a} \quad . \tag{A-3}$$

$\frac{\partial \phi}{\partial \eta}$ for interior points and for left-and right-boundary points:

$$\left.\frac{\partial \phi}{\partial \eta}\right|_P = \frac{\phi_N - \phi_S}{2b} \quad . \tag{A-4}$$

$\frac{\partial \phi}{\partial \eta}$ for upper-boundary points:

$$\left.\frac{\partial \phi}{\partial \eta}\right|_P = \frac{\phi_{SS} + 3\phi_P - 4\phi_S}{2b} \quad . \tag{A-5}$$

$\frac{\partial \phi}{\partial \eta}$ for lower-boundary points:

$$\left.\frac{\partial \phi}{\partial \eta}\right|_P = \frac{4\phi_N - \phi_{NN} - 3\phi_P}{2b} \quad . \tag{A-6}$$

$\frac{\partial^2 \phi}{\partial \xi^2}$ for interior points and for upper- and lower-boundary points:

$$\left.\frac{\partial^2 \phi}{\partial \xi^2}\right|_P = \frac{\phi_E - 2\phi_P + \phi_W}{a^2} \quad . \tag{A-7}$$

$\frac{\partial^2\phi}{\partial\xi^2}$ for left-boundary points:

$$\left.\frac{\partial^2\phi}{\partial\xi^2}\right|_P = \frac{4\phi_{EE} - \phi_{EEE} - 5\phi_E + 2\phi_P}{a^2} \quad . \tag{A-8}$$

$\frac{\partial^2\phi}{\partial\xi^2}$ for right-boundary points:

$$\left.\frac{\partial^2\phi}{\partial\xi^2}\right|_P = \frac{4\phi_{WW} - \phi_{WWW} - 5\phi_W + 2\phi_P}{a^2} \quad . \tag{A-9}$$

$\frac{\partial^2\phi}{\partial\eta^2}$ for interior points and for left- and right-boundary points:

$$\left.\frac{\partial^2\phi}{\partial\eta^2}\right|_P = \frac{\phi_N - 2\phi_P + \phi_S}{b^2} \quad . \tag{A-10}$$

$\frac{\partial^2\phi}{\partial\eta^2}$ for upper-boundary points:

$$\left.\frac{\partial^2\phi}{\partial\eta^2}\right|_P = \frac{4\phi_{SS} - \phi_{SSS} - 5\phi_S + 2\phi_P}{b^2} \quad . \tag{A-11}$$

$\frac{\partial^2\phi}{\partial\eta^2}$ for lower-boundary points:

$$\left.\frac{\partial^2\phi}{\partial\eta^2}\right|_P = \frac{4\phi_{NN} - \phi_{NNN} - 5\phi_N + 2\phi_P}{b^2} \quad . \tag{A-12}$$

$\frac{\partial^2\phi}{\partial\xi\partial\eta}$ for interior points:

$$\left.\frac{\partial^2\phi}{\partial\xi\partial\eta}\right|_P = \frac{\phi_{NE} - \phi_{SE} - \phi_{NW} + \phi_{SW}}{4ab} \quad . \tag{A-13}$$

$\frac{\partial^2\phi}{\partial\xi\partial\eta}$ for upper-boundary points:

$$\left.\frac{\partial^2\phi}{\partial\xi\partial\eta}\right|_P = \frac{3(\phi_E - \phi_W) + \phi_{SSE} - \phi_{SSW} - 4(\phi_{SE} - \phi_{SW})}{4ab} \quad . \tag{A-14}$$

$\frac{\partial^2\phi}{\partial\xi\partial\eta}$ for lower-boundary points:

$$\left.\frac{\partial^2\phi}{\partial\xi\partial\eta}\right|_P = \frac{4(\phi_{NE} - \phi_{NW}) - 3(\phi_E - \phi_W) - \phi_{NNE} + \phi_{NNW}}{4ab} \quad . \tag{A-15}$$

$\frac{\partial^2\phi}{\partial\xi\partial\eta}$ for left-boundary points:

$$\left.\frac{\partial^2\phi}{\partial\xi\partial\eta}\right|_P = \frac{4(\phi_{NE} - \phi_{SE}) - 3(\phi_N - \phi_S) - \phi_{NEE} + \phi_{SEE}}{4ab} \quad . \tag{A-16}$$

$\frac{\partial^2\phi}{\partial\xi\partial\eta}$ for right-boundary points:

$$\left.\frac{\partial^2\phi}{\partial\xi\partial\eta}\right|_P = \frac{3(\phi_N - \phi_S) + \phi_{NWW} - \phi_{SWW} - 4(\phi_{NW} - \phi_{SW})}{4ab} \quad . \tag{A-17}$$

At corner points, the difference approximations for the first derivatives at the perpendicular boundaries are combined to give the difference approximation for the mixed derivative.

APPENDIX B: DERIVATIVE FORMULAS FOR THE CONFORMAL MAPPING PROCEDURE

The derivative formulas expressed in terms of the computational plane coordinates that are used in the present analysis are given in this appendix.

$$\frac{\partial \phi}{\partial x} = \frac{\partial \mu}{\partial x}\frac{d\xi}{d\mu}\frac{\partial \phi}{\partial \xi} + \frac{\partial \lambda}{\partial x}\frac{\partial \eta}{d\lambda}\frac{\partial \phi}{\partial \eta} \quad . \tag{B-1}$$

$$\frac{\partial^2 \phi}{\partial x^2} = \left[\frac{\partial^2 \mu}{\partial x^2}\frac{d\xi}{d\mu} + \left(\frac{\partial \mu}{\partial x}\right)^2 \frac{d^2 \xi}{d\mu^2}\right]\frac{\partial \phi}{\partial \xi} + \left(\frac{\partial \mu}{\partial x}\frac{d\xi}{d\mu}\right)^2 \frac{\partial^2 \phi}{\partial \xi^2}$$

$$+ 2\left(\frac{\partial \mu}{\partial x}\frac{\partial \lambda}{\partial x}\frac{d\xi}{d\mu}\frac{d\eta}{d\lambda}\right)\frac{\partial^2 \phi}{\partial \xi \partial \eta} + \left[\frac{\partial^2 \lambda}{\partial x^2}\frac{d\eta}{d\lambda} + \left(\frac{d\lambda}{\partial x}\right)^2 \frac{d^2 \eta}{d\lambda^2}\right]\frac{\partial \phi}{\partial \eta} \tag{B-2}$$

$$+ \left(\frac{\partial \lambda}{\partial x}\frac{d\eta}{d\lambda}\right)^2 \frac{\partial^2 \phi}{\partial \eta^2} \quad . \tag{B-2}$$

$$\frac{\partial \phi}{\partial y} = -\frac{\partial \lambda}{\partial x}\frac{d\xi}{d\mu}\frac{\partial \phi}{\partial \xi} + \frac{\partial \mu}{\partial x}\frac{d\eta}{d\lambda}\frac{\partial \phi}{\partial \eta} \quad . \tag{B-3}$$

$$\frac{\partial^2 \phi}{\partial y^2} = \left[-\frac{\partial^2 \mu}{\partial x^2}\frac{d\xi}{d\mu} + \left(\frac{\partial \lambda}{\partial x}\right)^2 \frac{d^2 \xi}{d\mu^2}\right]\frac{\partial \phi}{\partial \xi} + \left(\frac{\partial \lambda}{\partial x}\frac{d\xi}{d\mu}\right)^2 \frac{\partial^2 \phi}{\partial \xi^2}$$

$$- 2\left[\frac{\partial \lambda}{\partial x}\frac{\partial \mu}{\partial x}\frac{d\xi}{d\mu}\frac{d\eta}{d\lambda}\right]\frac{\partial^2 \phi}{\partial \xi \partial \eta} + \left[-\frac{\partial^2 \lambda}{\partial x^2}\frac{d\eta}{d\lambda} + \left(\frac{\partial \mu}{\partial x}\right)^2 \frac{d^2 \eta}{d\lambda^2}\right]\frac{\partial \phi}{\partial \eta}$$

$$+ \left(\frac{\partial \mu}{\partial x}\frac{d\eta}{d\lambda}\right)^2 \frac{\partial^2 \phi}{\partial \eta^2} \quad . \tag{B-4}$$

$$\frac{\partial^2\phi}{\partial x\partial y} = -\left[\frac{\partial^2\lambda}{\partial x^2}\frac{d\xi}{d\mu} + \frac{\partial\mu}{\partial x}\frac{\partial\lambda}{\partial x}\frac{d^2\xi}{d\mu^2}\right]\frac{\partial\phi}{\partial\xi} - \frac{\partial\mu}{\partial x}\frac{\partial\lambda}{\partial x}\left(\frac{d\xi}{d\mu}\right)^2\frac{\partial^2\phi}{\partial\xi^2}$$

$$+\left[\left(\frac{\partial\mu}{\partial x}\right)^2 - \left(\frac{\partial\lambda}{\partial x}\right)^2\right]\frac{d\xi}{d\mu}\frac{d\eta}{d\lambda}\frac{\partial^2\phi}{\partial\xi\partial\eta} + \left(\frac{\partial^2\mu}{\partial x^2}\frac{d\eta}{d\lambda} + \frac{\partial\lambda}{\partial x}\frac{\partial\mu}{\partial x}\frac{d^2\eta}{d\lambda^2}\right)\frac{\partial\phi}{\partial\eta}$$

$$+\frac{\partial\lambda}{\partial x}\frac{\partial\mu}{\partial x}\left(\frac{d\eta}{d\lambda}\right)^2\frac{\partial^2\phi}{\partial\eta^2} \quad . \qquad \text{(B-5)}$$

NOMENCLATURE

A_D	empirical constant in turbulence model
A_E, A_W, A_N, A_S, A_P	coefficients in discretized form of the Poisson equation
A_μ	empirical constant in turbulence model
a	finite-difference node spacing in ξ direction
B_P	source term in discretized form of the Poisson equation
b	finite-difference node spacing in η direction
C_D	empirical constant in turbulence model
C_E, C_W, C_N, C_S, C_P	coefficients in discretized form of the transport equation
c_μ	empirical constant in turbulence model
D	jet slot width at entrance plane to solution domain
D_P	source term in discretized form of the transport equation
d_n	nozzle exit diameter in the free-upper-boundary geometry
E, EE, EEE	east points in the finite-difference grid
F	conformal mapping function
f_1, f_2	stretching functions
f_i, i = 1, ...,10	functions specifying boundary conditions
g	ratio of finite-difference node spacings, a/b
H	height of jet entrance plane above ground (height of computational plane)
h	function describing curved-plate geometry
i	$\sqrt{-1}$
k	turbulent kinetic energy
L_E, L_W, L_N, L_S, L_P	coefficients in the discretized form of the Laplace equation
ℓ, ℓ_1, ℓ_2	geometric length scales
ℓ_D	length scale for dissipation

ℓ_μ	length scale for viscosity
N, NN, NNN	north points in the finite-difference grid
NE, NNE, NEE	northeast points in the finite-difference grid
NW, NNW, NWW	northwest points in the finite-difference grid
P	central point in the finite-difference grid
p	static pressure
Q	mapping modulus
Re	Reynolds number based on jet properties at entrance plane to solution domain
S, SS, SSS	south points in the finite-difference grid
SE, SSE, SEE	southeast points in the finite-difference grid
SW, SSW, SWW	southwest points in the finite-difference grid
u	velocity component in x direction
u_i	velocity vector
V_o	jet centerline velocity at entrance plane to solution domain
v	velocity component in y direction
W	width of computational plane
W'	half-width of the upper boundary of the physical plane
W, WW, WWW	west points in the finite-difference grid
x	cartesian coordinate for plane flow
x_i	general cartesian coordinate
y	cartesian coordinate for plane flow
α	coefficient in general form of the transport equation
β	coefficient in general form of the transport equation; parameter in conformal mapping test case
$\Gamma_{k,eff}$	effective transfer coefficient for diffusion
γ	coefficient in general form of the transport equation
δ	coefficient in general form of the transport equation
η	computational plane coordinate
θ	jet vector angle
θ_1, θ_3	contributions to source term in discretized form of the transport equation

κ	turbulent (eddy) viscosity
λ	mapping plane coordinate
μ	molecular viscosity; mapping plane coordinate
μ_{eff}	effective viscosity
μ_{turb}	turbulent (eddy) viscosity
ν	kinematic molecular viscosity
ξ	computational plane coordinate
ρ	mass density
σ_k	molecular Prandtl number
$\sigma_{k,turb}$	turbulent Prandtl number
σ_P	source term in the Poisson equation
σ_T	source term in the transport equation
$\tau_{i,\ i\ =\ 1,\ 2,\ 3}$	coefficients in the transport equation
$\tau_{i,j}$	stress tensor
ϕ	general flow variable
ψ	stream function
ω	vorticity
$\bar{\ }$	dimensional quantity
$\langle\ \rangle$	time-averaged quantity
	fluctuating component

DISTRIBUTION LIST

Addressees	Cys
Chief of Naval Research Department of the Navy Arlington, VA 22217 ATTN: Vehicle Technology Program, Code 211	5
Code 430B	1
Chief of Naval Development Department of the Navy Washington, DC 20360 ATTN: NAVMAT 0331	1
NAVMAT 0334	1
Naval Air Systems Command Department of the Navy Washington, DC 20351 ATTN: NAVAIR 320D	1
NAVAIR 5301	1
NAVAIR 53013	1
David Taylor Naval Ship Research & Development Center Bethesda, MD 20084 ATTN: Code 16	1
Code 522.3	1
Code 522.1	1
Naval Research Laboratory Washington, DC 20375 ATTN: Technical Information Office, Code 2627	1
Library, Code 2629	1
Superintendent U. S. Naval Academy Annapolis, MD 21402	1
Superintendent U. S. Naval Postgraduate School Monterey, CA 93940	1
U. S. Naval Air Development Center Warminster, PA 18974 Air Vehicle Technology Dept. ATTN: Code 301	1
ONR Branch Office 1030 East Green Street Pasadena, CA 91106 ATTN: Mr. B. F. Cagle	1
ONR Branch Office 495 Summer Street Boston, MA 02210 ATTN: Dr. A. D. Wood	1
ONR Branch Office 536 South Clark Street Chicago, IL 60605 ATTN: Mr. M. A. Chaszeyka	1
Commandant of the Marine Corps Washington, DC 20380 ATTN: Dr. A. L. Slafkosky Scientific Advisor (Code RD-1)	1
Defense Documentation Center Cameron Station, Bldg. 5 Alexandria, VA 22314	12
Department of the Army DCS for Research and Development and Acquisition Washington, DC 20310 ATTN: DAMA-WSA (Mr. R. L. Ballard)	1
U. S. Army Material Command 5001 Eisenhower Avenue Alexandria, VA 22333 ATTN: AMCRD-F	1
Director, Headquarters U. S. Army Air Mobility R&D Lab. Ames Research Center Moffett Field, CA 94035	1
Director, Ames Directorate U. S. Army Air Mobility R&D Lab. Ames Research Center Moffett Field, CA 94035	1

Addressees	Cys
Director, Langley Directorate U. S. Army Air Mobility R&D Lab. Langley Research Center Hampton, VA 23665	1
Director, Eustis Directorate U. S. Army Mobility R&D Lab. Fort Eustis, VA 23604	1
U. S. Air Force Flight Dynamics Laboratory Wright-Patterson AFB, OH 45433	
ATTN: PT, Prototype Division	1
FXM, Aeromechanics Branch	1
Air Force Office of Scientific Research Directorate of Aerospace Sciences Bolling AFB, DC 20332	1
National Aeronautics and Space Administration 600 Independence Avenue, SW Washington, DC 20546	
ATTN: Code RAA	1
Code RAV	1
National Aeronautics and Space Administration Ames Research Center Moffett Field, CA 94035	
ATTN: Dr. T. Gregory, FAE	1
Dr. G. Chapman, FAR	1
National Aerodynamics and Space Administration Langley Research Center Hampton, VA 23665 Subsonic, Transonic Aerodynamics Div.	
ATTN: Dr. James F. Campbell	1
DCW Industries 4367 Troost Avenue Studio City, CA 91604	1

Addressees	Cys
Lockheed Missiles & Space Co., Inc. Huntsville Research & Engineering Center P. O. Box 1103 Huntsville, AL 35807	
ATTN: Mr. A. Zalay	1
Nielsen Engineering & Research, Inc. 510 Clyde Avenue Mountain View, CA 94043	1
General Dynamics/Fort Worth Division P. O. Box 748 Fort Worth, TX 76101 Mail Zone 2882	
ATTN: R. W. Woodrey	1
Lockheed-Georgia Company Department 72-74, Zone 403 Marietta, GA 30063	
ATTN: Mr. Charles Dixon	1
Rockwell International Columbus Aircraft Division 4300 East Fifth Avenue P. O. Box 1259 Columbus, OH 43216	
ATTN: Dr. P. Bevilaqua	1
Analytical Methods, Inc. 100 - 116th Avenue, S.E. Bellevue, WA 98004	
ATTN: Dr. F. Dvorak	1
Grumman Aerospace Corporation Bethpage, NY 11714 Research Department	
ATTN: Dr. R. Melnik	1
Dr. R. Oman	1
Advanced Development Department	
ATTN: Mr. R. Hadcock	1

Addressees	Cys
Vought Corporation Advanced Technology Center P. O. Box 6144 Dallas, TX 75222 ATTN: Mr. H. H. Driggers	1
University of Cincinnati Dept. of Aerospace Engineering and Applied Mechanics Cincinnati, OH 45221 ATTN: Dr. R. T. Davis	1
New York University Courant Inst. of Mathematical Sciences 251 Mercer Street New York, NY 10012 ATTN: Dr. A. Jameson	1
Virginia Polytechnic Institute & State University Aerospace & Ocean Engineering Dept. Blacksburg, VA 22030 ATTN: Dr. C. Lewis	1
Massachusetts Institute of Technology Dept. of Aeronautics and Astronautics Cambridge, MA 02139 ATTN: Prof. Rene Miller Prof. Norman Ham	1 1
National Aeronautics and Space Administration Ames Research Center Moffett Field, CA 94035 ATTN: David H. Hickey FSA, Code 247-1	1
National Aeronautics and Space Administration Langley Research Center Hampton, VA 23665 ATTN: Richard J. Margason, Code 286	1

Addressees	Cys
U. S. Naval Air Development Center Warminster, PA 18974 ATTN: John D. Ctrus, Code 3014 C. Mazza, Code 3015	1 1